



Equatorial Waves Triggering Extreme Rainfall and Floods in Southwest Sulawesi, Indonesia

BEATA LATOS,^a THIERRY LEFORT,^b MARIA K. FLATAU,^c PIOTR J. FLATAU,^d DONALDI S. PERMANA,^e DARIUSZ B. BARANOWSKI,^a JAKA A. I. PASKI,^e ERWIN MAKMUR,^e EKO SULYSTYO,^e PHILIPPE PEYRILLÉ,^f ZHE FENG,^g ADRIAN J. MATTHEWS,^h AND JEROME M. SCHMIDT^c

^a Institute of Geophysics, Polish Academy of Sciences, Warsaw, Poland

^b École Nationale de la Météorologie, Météo-France, Toulouse, France

^c Naval Research Laboratory, Monterey, California

^d Scripps Institution of Oceanography, University of California, San Diego, San Diego, California

^e Agency for Meteorology, Climatology and Geophysics of the Republic of Indonesia, Jakarta, Indonesia

^f Centre National de Recherches Météorologiques, Météo-France, Toulouse, France

^g Pacific Northwest National Laboratory, Richland, Washington

^h Centre for Ocean and Atmospheric Sciences, School of Environmental Sciences, and School of Mathematics, University of East Anglia, Norwich, United Kingdom

(Manuscript received 17 August 2020, in final form 2 February 2021)

ABSTRACT: On the basis of detailed analysis of a case study and long-term climatology, it is shown that equatorial waves and their interactions serve as precursors for extreme rain and flood events in the central Maritime Continent region of southwest Sulawesi, Indonesia. Meteorological conditions on 22 January 2019 leading to heavy rainfall and devastating flooding in this area are studied. It is shown that a convectively coupled Kelvin wave (CCKW) and a convectively coupled equatorial Rossby wave (CCERW) embedded within the larger-scale envelope of the Madden-Julian oscillation (MJO) enhanced convective phase, contributed to the onset of a mesoscale convective system that developed over the Java Sea. Low-level convergence from the CCKW forced mesoscale convective organization and orographic ascent of moist air over the slopes of southwest Sulawesi. Climatological analysis shows that 92% of December–February floods and 76% of extreme rain events in this region were immediately preceded by positive low-level westerly wind anomalies. It is estimated that both CCKWs and CCERWs propagating over Sulawesi double the chance of floods and extreme rain event development, while the probability of such hazardous events occurring during their combined activity is 8 times greater than on a random day. While the MJO is a key component shaping tropical atmospheric variability, it is shown that its usefulness as a single factor for extreme weather-driven hazard prediction is limited.

KEYWORDS: Maritime Continent; Kelvin waves; Madden-Julian oscillation; Extreme events; Flood events; Precipitation

1. Introduction

Indonesia, with its tropical and monsoonal climate, is exposed to extreme rain accumulation (Ramage 1968; Chang et al. 2005; Moron et al. 2015) and thus weather-driven hazards, such as landslides (Liao et al. 2010) and floods (Aryastana et al. 2015; Sekaranom and Masunaga 2017; Sugiartha et al. 2017; Paski et al. 2020). Population growth, deforestation and significant changes in land use have resulted in shrinking retention areas, which along with climate change make the country especially vulnerable to flooding (Measey 2010; Muis et al. 2015). Official statistics published by the Indonesian National Agency for Disaster Countermeasure (BNPB) indicate that

between 2010 and 2018, around 87% of all natural disasters nationwide were hydrometeorological events (including floods, tides, tornadoes, droughts, and landslides) and 36% of all natural disasters were floods (BNPB 2019). However, physical phenomena triggering extreme rainfall and weather-driven hazards still remain to be fully investigated. This lack of understanding is challenging, especially from the socioeconomic perspective of a developing country (Jongman et al. 2015).

Sulawesi (Fig. 1) is the fourth largest and third most populated of the Indonesian islands. It is located east of Borneo, between the Java Sea to the southwest, the Celebes Sea to the north, and the Banda Sea to the east. Sulawesi is inhabited by nearly 20 million people. Nearly 9 million people, or about 45% of the island's population, live in the densely populated South Sulawesi province located in the southwestern part of the island. Makassar is the capital and the largest urban area of the

Corresponding author: Beata Latos, blatos@igf.edu.pl

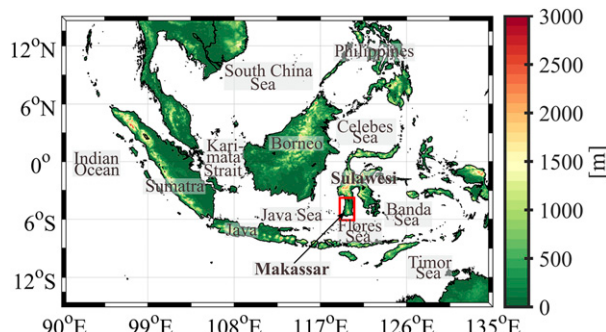


FIG. 1. Orography (m) of the western and central Maritime Continent. Significant locations referred to in the main text are marked. The red box indicates the domain around southwest Sulawesi shown in Fig. 2.

island, as well as the eighth biggest city in Indonesia with a population of nearly 1.5 million (Central Bureau of Statistics 2017). The city is located west of a mountain chain and is adjacent to the Java Sea. This area constitutes the southwestern Sulawesi region, which is particularly prone to flooding. In this region between 1999 and 2018, nearly half of all natural disasters (46%) were floods (BNPB 2019). In January 2019, southwest Sulawesi, including Makassar, experienced its largest flood on record. The goal of this work is to understand the large-scale meteorological conditions associated with this flood and with other flooding events in this region.

Indonesia constitutes the largest part of the Maritime Continent (MC), an area of ocean and islands within the Indo-Pacific warm pool in Southeast Asia, which represents the largest area of very high sea surface temperatures on Earth. It is a major center of atmospheric convection accompanied by significant latent heat release (Ramage 1968; Simpson et al. 1993). The combination of land and ocean areas with local and large-scale drivers of convection makes weather forecasting in this area a challenging task (Love et al. 2011; Birch et al. 2016; Johnson et al. 2016; Baranowski et al. 2019) and limits the predictability of heavy rain events. The climate of southwest Sulawesi (Gowa, Makassar, Maros, Jeneponto, and Takalar districts) is monsoonal with two main seasons: a wet season between November and April, with prevailing westerly winds, and a dry season throughout the rest of the year.

Precipitation over the MC region has a multiscale character; it varies in response to a number of large-scale phenomena. Over a long, interannual time scale, regional precipitation patterns are modified by climate modes such as El Niño–Southern Oscillation (ENSO) (Aldrian and Dwi Susanto 2003; Jia et al. 2016; Zhang et al. 2016) or the Indian Ocean dipole (IOD) (Saji et al. 1999; Schott et al. 2009). On an intra-annual time scale, rainfall variability is associated with the seasonal progression of the intertropical convergence zone (ITCZ) and monsoonal flow. Over Sulawesi, the Southeast Asian monsoon provides an environment supportive of rain events (Kripalani and Kulkarni 1997; Chang et al. 2005) during the boreal winter. On a subseasonal time scale, convection over the MC is to a great extent driven by large-scale propagating modes such as the Madden–Julian oscillation (MJO) (Madden and Julian 1972; Peatman et al. 2014), which is a dominant component of intraseasonal variability in the tropics

(Zhang 2005), and equatorially trapped convectively coupled waves (Wheeler and Kiladis 1999; Kiladis et al. 2009), that contribute up to 16%–20% of total intraseasonal precipitation (Lubis and Jacobi 2015). In particular, eastward-propagating convectively coupled Kelvin waves (CCKWs) have high amplitude over the Maritime Continent (Roundy 2008; Baranowski et al. 2016b). Together with other equatorial waves, they form the “building blocks” of the active phase of the MJO (Majda et al. 2004; Wheeler and Nguyen 2015).

Recent studies (Chen et al. 2019) show that CCKWs have an impact on rainfall variability over the greater part of the MC and can provide useful guidance for weather forecasting in this region, even in the absence of an active MJO. For example, in Sumatra, CCKWs constitute a critical dynamical predictor for flood onset (Baranowski et al. 2020) – this mode is associated with over 90% of all floods and is solely responsible for nearly 30% of them. Similarly, Lubis and Respati (2021) show that the convectively active phases of Kelvin waves increase the probability of extreme rain events over Java Island by about 30%–60%. On the other hand, the convectively active phases of Rossby waves increase the probability by about 15%–45%. Ferrett et al. (2019) also links extreme precipitation (exceeding 95th percentile of precipitation for 1998–2016), both in the western and eastern part of the Maritime Continent, to equatorial waves. In their study, the largest increase in rainfall in Indonesia, including Sulawesi, was primarily associated with high-amplitude CCKWs. On a shorter, synoptic time scale, extreme precipitation events and floods in the western MC have been associated with cold surges and with the Borneo vortex (Tangang et al. 2008; Salahuddin and Curtis 2011; Lim et al. 2017; Paulus and Shanas 2017).

In addition, precipitation on the MC islands and in their offshore vicinity is driven by a very strong diurnal cycle of local convection and circulation (Qian 2008; Yamanaka et al. 2018; Paski et al. 2019; Sakaeda et al. 2020). Diurnal land convection influences the Maritime Continent response to MJO propagation, with enhanced precipitation over the large islands developing ahead of the MJO-related convection over the ocean (Peatman et al. 2014; Sakaeda et al. 2020; Qian 2020). In turn, the diurnal cycle influences longer-time-scale variability and mean precipitation through an upscale energy transfer (Birch et al. 2016; Ruppert and Chen 2020). Therefore, precipitation variability over the entire MC region, including the island of Sulawesi, has a fully multiscale character.

This paper attempts to establish a link between extreme rainfall, floods in southwest Sulawesi, and their meteorological drivers. The structure of the paper is as follows: section 2 presents the datasets and methods used, section 3 describes the rainfall drivers of the January 2019 Makassar flood, section 4 explores the statistical relationship between floods and extreme rainfall and gives insight into their connection with equatorial waves, and section 5 provides the summary and conclusions.

2. Data and methods

a. Satellite data

Gridded daily outgoing longwave radiation (OLR) (Liebmann and Smith 1996) on a regular $2.5^\circ \times 2.5^\circ$ latitude–longitude grid for the 1 January 1998–30 June 2019 period was used. Daily

precipitation estimates (combined microwave-IR) based on the 3-hourly Tropical Rainfall Measuring Mission (TRMM) (Huffman et al. 2010) gridded dataset (TRMM 3B42 v7) were utilized at their native spatial resolution of 0.25° for the same period as the OLR data. Additionally, Integrated Multisatellite Retrievals for Global Precipitation Mission (IMERG) Final Precipitation L3 V06 products (Huffman et al. 2019) on a $0.1^\circ \times 0.1^\circ$ latitude-longitude grid were used, daily and half-hourly for the 19–24 January 2019 period and half-hourly for 1 October 2013–30 June 2019.

b. Reanalysis data

European Centre for Medium-Range Weather Forecasts (ECMWF) fifth major global reanalysis (ERA5) data (zonal and meridional wind and specific humidity) for the 19–24 January 2019 period were obtained at 20 pressure levels between 1000 and 300 hPa on a regular $0.25^\circ \times 0.25^\circ$ latitude-longitude grid with hourly temporal resolution, and for the 1 October 2018–30 June 2019 period with daily resolution (Copernicus Climate Change Service (C3S) 2017). Additionally, the horizontal divergence of velocity for January 2019 were obtained at 27 pressure levels between 1000 and 100 hPa. The 850-hPa zonal and meridional wind components were obtained for the 1 January 1998–30 June 2019 period to calculate climatologies of lower-tropospheric winds. Finally, ERA5 relative vorticity at 500 mb was obtained for 21 and 22 January 2019.

c. In situ data

Daily rainfall measurements for the period 20–23 January 2019 were obtained from 22 stations located in southwest Sulawesi, in the districts of Makassar, Maros, and Gowa. Daily rain accumulation, average wind speed at 10 m above the ground and sunshine duration between 1 January 1999 and 30 June 2019 were obtained for Maros Climatological Station (WMO ID 97184) and Hasanuddin Meteorological Station, located in Makassar (WMO ID 97180). The data are available at <http://dataonline.bmkg.go.id> – an online database developed by the Agency for Meteorology, Climatology and Geophysics of the Republic of Indonesia (BMKG 2019). Twice-daily weather balloon data were obtained for Ujung Pandang (Makassar) WMO station number 97180. Missing data on 3, 4, 5, 10, 22, and 28 of January and upper-level data on days when the balloon burst below 50 hPa were estimated using linear interpolation.

d. Sea surface temperature data

Sea surface temperature (SST) data from the Fleet Numerical Meteorology and Oceanography Center (FNMONC) High-Resolution SST/Sea Ice Analysis for Global High Resolution SST project were used (GHRSST 2019). Data are available every 6 h at a near-global Mercator projection grid, with 12-km resolution at the equator. Data for 1 January 2006–31 January 2019 were used to calculate SST anomalies in January 2019, during the Makassar flood.

e. Water vapor transport

The integrated horizontal water vapor transport (IVT) was calculated using ERA5 zonal and meridional winds and specific humidity:

$$\text{IVT} = \left[\left(\frac{1}{g} \int_{1000}^{300} qu dp \right)^2 + \left(\frac{1}{g} \int_{1000}^{300} qv dp \right)^2 \right]^{1/2}, \quad (1)$$

where q , g , p , u , and v represent specific humidity, acceleration due to gravity, pressure, and zonal and meridional wind speed, respectively. The integral was calculated between 1000 and 300 hPa, using 20 levels of the ERA5 dataset.

f. Calculation of daily anomalies

Daily anomalies of relevant data (ERA5, OLR, TRMM, in situ) were computed by removing the seasonal cycle, defined as the mean plus the first three annual harmonics fitted to an average annual cycle calculated for the 1998–2019 period. Due to data availability, SST anomalies for January 2019 were defined as the difference from average January conditions calculated between 2006 and 2019.

g. Equatorial wave filtering

To isolate signals associated with distinct equatorial modes, a wavenumber-frequency spectral analysis (Wheeler and Kiladis 1999, hereafter WK99) was performed for all latitudes in the meridional band of 15°S – 15°N , using the NCAR command language (NCL) script filter_waves, available from Dr. C. Schreck at GitLab (https://k3.cicsnc.org/carl/carl-ncl-tools/blob/master/filter/filter_waves.ncl). For each latitude within these bounds, a two-dimensional fast Fourier transform (FFT) was performed in longitude and time dimensions on daily anomalies with the annual cycle removed, to transform to wavenumber-frequency space. Filtering was then applied to isolate variability corresponding to each mode and the data were transformed back to physical, longitude-time space. The wavenumber-frequency filtering for the MJO mode retained eastward-propagating signals with zonal wavenumbers 1–9 and periods of 30–96 days (Kiladis et al. 2005). CCKWs were defined as propagating signals with equivalent depths of 8–90 m, periods of 2.5–17 days, and eastward propagation at zonal wavenumbers 1–14 (Straub and Kiladis 2002). Rossby waves were defined as westward-propagating disturbances with zonal wavenumbers 1–10, periods 9.7–48 days, and equivalent depths of 5–9 m (Kiladis et al. 2009).

Although the original WK99 method chooses the wavenumber-frequency band for each wave according to the power spectrum of OLR, it is also applicable to other parameters, such as precipitation (e.g., Lubis and Jacobi 2015; Guo et al. 2014; Baranowski et al. 2016a; Sakaeda et al. 2020), wind fields (e.g., Ridout and Flatau 2011; Chen et al. 2019), as well as precipitable water (e.g., Roundy and Frank 2004). The structure of precipitation and wind fields resembles the expected structure of equatorial waves (see section 4b; Fig. 13 for details).

h. Radar data and analysis

The Gematronik C-band Doppler radar located in Maros (4.9977°S , 119.5720°E , 19 m MSL) was used to derive the high-resolution local rainfall field for 20–23 January 2019 period (the radar stopped operating for about 3 h on 22 January due to a power outage during the flood). The data were recorded every 10 min in volumetric format, consisting of nine plan

position indicator (PPI) scans containing reflectivity values in decibels (dBZ).

Radar data processing was conducted using the wradlib Python library (Heistermann et al. 2013), which includes reading common data formats, georeferencing, identifying and correcting typical error sources (such as clutter or attenuation), converting reflectivity to rainfall intensity, and data visualization. Elimination of ground clutter, caused by nonmeteorological factors, such as the presence of objects on the surface of Earth (e.g., mountains, hills, tall buildings) or objects in the air (e.g., aircraft or birds) was done by texture-based technique developed by Gabella and Notarpietro (2002). Afterward, the attenuation correction was applied using methods developed by Krämer and Verworn (2009). The approach accounts for the microphysical properties of current rainfall, rather than adjustment of radar data with the help of rain gauges. For each volumetric file, the altitude column maximum of PPI (CMAX) was extracted and finally, converted into NetCDF format in Cartesian coordinates. Following methods used by BMKG, the quantitative precipitation estimation (QPE) value was derived from the following Z–R relationship: $Z = AR^b$, where $A = 200$, $b = 1.6$, Z is the reflectivity factor, and R is the rainfall rate (Marshall et al. 1947).

i. Tracking of mesoscale convective systems and high-frequency precipitation events

An updated version of the FLEXible object TRaKeR (FLEXTRKR) algorithm (Feng et al. 2018) was employed to track mesoscale convective systems (MCSs) in December, January, and February 2014–19 over the MC region based on NASA global MergedIR infrared brightness temperature data (Janowiak et al. 2001) and GPM IMERG half-hourly precipitation data (Huffman et al. 2014). The method is described in detail in Feng et al. (2021). At first, the method identifies and tracks large cold cloud systems (CCS) associated with deep convection using satellite infrared (Tb) data and subsequently identifies MCSs using GPM IMERG precipitation feature (PF) characteristics. An MCS is defined as a large CCS ($Tb < 241\text{ K}$, area $> 4 \times 10^4\text{ km}^2$) that contains a PF (contiguous area within a CCS with rain rate $> 2\text{ mm h}^{-1}$) with major axis length $> 100\text{ km}$, and PF area, PF mean rain rate, PF rain-rate skewness, and heavy rain (rain rate $> 10\text{ mm h}^{-1}$) volume ratio exceeding certain thresholds and which persists for at least 5 h.

High-frequency (HF) precipitation events between 1998 and 2019 were identified using a 3-hourly TRMM gridded dataset. First, HF precipitation signal is defined using a high-pass time filter that retains signal with frequencies higher than 3 days. Next, HF signal is spatially averaged over southwestern Sulawesi. HF precipitation events are defined as events for which normalized precipitation continuously, for a period longer than 12 h, exceeds two, three, or four standard deviations calculated for the entire 1999–2019 period.

j. Floods database

A database of flood events was obtained from the Indonesian National Agency for Disaster Countermeasure (BNPB) at <http://dibi.bnbp.go.id/> for southwest Sulawesi (area of 4975 km^2). Most (66 out of 80) of the flood events between 1 January 1999–28 February 2019 in this database occurred

during the boreal winter months (DJF). Within the southwest Sulawesi region, there are five administrative regencies: Gowa (1883 km^2), Makassar (199 km^2), Maros (1619 km^2), Jeneponto (707 km^2), and Takalar (567 km^2). The database contained repetitions because each regency reports floods separately. Thus, a flood event on a particular day can be reported up to five times. To resolve this issue, we ignored events that were repeated. This led to 42 flood events, out of which we disregarded 3 cases of very low (less than 35 mm) 4-day precipitation accumulation estimated using the TRMM dataset. In the end, we obtained 39 DJF flooding days with substantial precipitation, which occurred between 1 January 1999 and 28 February 2019.

k. Extreme rainfall database

To explore the distribution of extreme rainfall, we used mean values of in situ data from two stations with continuous, high-quality precipitation records (Maros Climatological Station and Hasanuddin Meteorological Station). Following the definition adopted by BMKG, days with in situ-measured rain accumulation exceeding 100 mm (an average of two stations) were classified as “extreme rainfall days.” This absolute threshold corresponded to the 97th percentile of daily rainfall total, at each of the two stations. The timespan was set for DJF days between 1 January 1999 and 28 February 2019 to be consistent with the flood database period. By using this approach, we identified 49 extreme rain days.

3. Case study of devastating flood of January 2019

a. Flood event

In January 2019, the Jeneberang River overflowed its banks and caused a flood that was the most devastating ever reported in the region (BNPB 2019), with a total area affected by flooding at around 3700 km^2 . The total number of victims was estimated at 53 dead, 47 injured, and 14 085 evacuated (BNPB 2019).

The Jeneberang River basin is located in southwest Sulawesi, with its origin at 2833 m above mean sea level and its outflow at the city of Makassar into the Makassar Strait (Fig. 2). The river is 90 km long with a catchment area of 727 km^2 (Pawitan et al. 2002). To supply surrounding areas with year-round water and to prevent flooding, the Bili-Bili dam with a total capacity of $375\,000\,000\text{ m}^3$ has been constructed (Arafat et al. 2015). The Jeneberang River provides water for agricultural and urban needs, yet has a long history of flooding.

At 1600 UTC 20 January, precipitation began in southwest Sulawesi. Rain continued until 0800 UTC 23 January (Fig. 3). In many areas it brought continuous rain of up to 63-h duration. Local floods in the Jeneberang River basin started just after heavy rain began on 21 January. The rain caused an increase in the water level of the Jeneberang River and of the Bili-Bili dam. At 0600 UTC 21 January 2019, the water reached a critical level of 99.4 m and the reservoir operation door was opened. At the same time a warning was issued (PUPR 2019). The water level of the Bili-Bili dam continued to rise until 1200 UTC 22 January, when it reached the maximum of 101.6 m (PUPR 2019). On 22 January, the magnitude of this flood in Makassar was such that roads became impassable and power outages occurred. This was caused by continuous precipitation and the opening of the dam.

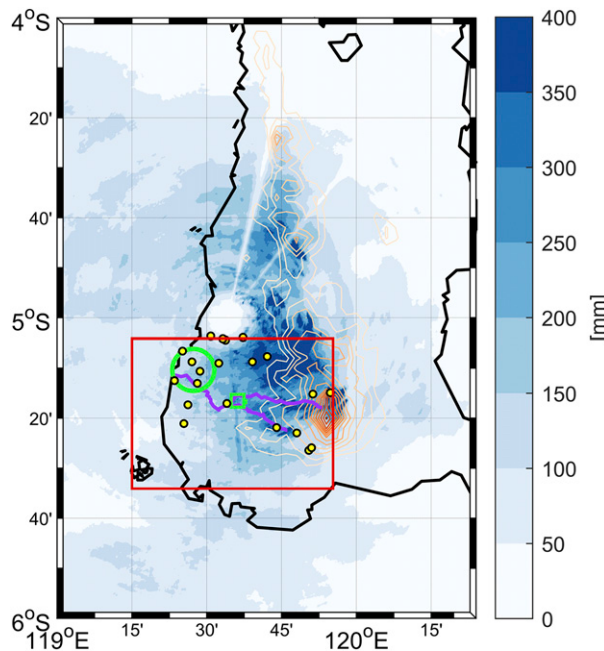


FIG. 2. Total precipitation (mm) estimated by a C-band Doppler radar located in Maros during 20–23 Jan 2019 (shading, interval: 50 mm), together with topography of the area (contours, interval: 200 m, from yellow at 400 m to brown at 3000 m). Location of the city of Makassar is qualitatively depicted by a green circle and Bili-Bili dam is indicated by a green rectangle. Locations of rain gauge stations are depicted by yellow circles. The red box shows the flood zone analyzed in Fig. 3. The Jeneberang River is marked with a purple line.

Radar observations (Fig. 2; animation of precipitation from C-band Doppler radar can be found by following the link: <https://doi.org/10.6084/m9.figshare.12758741.v1> (Latos and Permana 2020)) on 21 January and corresponding *Himawari-8* satellite images (not shown), indicate heavy onshore showers that started just after 0000 UTC. During the hours that followed, showers were mostly confined to the slopes of mountains. Lightning strikes were observed. At 1500 UTC 21 January, more widespread rain came from offshore convective systems and fewer lightning strikes were detected. The highest precipitation amounts were recorded around 0000 UTC 22 January (morning local time) (Fig. 3).

The total rainfall accumulated between 20 and 23 January in the flood zone (Fig. 2) reached 151 mm, based on radar measurements, 233 mm based on GPM satellite data and 376 mm according to in situ measurements (Fig. 3). The radar estimates are low in comparison to in situ and satellite observations. On 22 and 23 January, this may be related to a 3-hourly power outage at the radar site during the flood. Additionally, some uncertainty of Z-R QPE is expected, due to calibration, attenuation correction, Z-R relationship itself, etc. Rain gauges recorded the highest daily accumulation for each day except on 23 January, when GPM slightly exceeded the in situ measurements. Between 20 and 23 January, precipitation estimated by GPM data were 38% lower than measured by local rain gauges.

The GPM mission is the successor of TRMM, which was known to underestimate precipitation in mountainous regions (e.g., Berg et al. 2006; Huffman et al. 2010; Condom et al. 2011; Matthews et al. 2013; Rauniyar et al. 2017). GPM precipitation estimates are generally more accurate than TRMM, but the highest intensity rainfall in the MC is still underestimated (Mahmud et al. 2017). This is consistent with the results found here over the rapidly changing slope angle and surface heterogeneity of southwest Sulawesi.

The total rain accumulation from radar estimates between 20 and 23 of January is shown in Fig. 2. Over the mountain slopes of Jeneberang River basin, precipitation reached 350–400 mm. This is higher in comparison to values observed for the low-lying city of Makassar.

c. Synoptic overview

On 19 and 20 January, a pair of westward-moving cyclonic vortices was present over the eastern Maritime Continent (Fig. 4)—one in the Northern Hemisphere near the Philippines (on 20 January located around 8°N, 130°E) and the other in the Southern Hemisphere over the Timor Sea (on 20 January located around 10°S, 132°E). These twin vortices developed in the Pacific Ocean and propagated westward toward the MC. In addition, a pair of lee cyclonic vortices developed over the Indian Ocean near the western coast of Sumatra (on 20 January located around 3°N, 85°E and 12°S, 98°E)—Sumatra vortices (Fine et al. 2016), with increased westerly winds on the equator, near the Sumatra coast. On 21 January, a cold-surge-like wind pattern with a northerly component to the flow began to develop over the South China Sea, to the west of the Philippines. This reached the central South China Sea on 22 January and is further investigated in section 3f. On 21 January a westerly low-level jet (LLJ) developed over the Java Sea. The peak strength at 850 hPa (about 24 m s^{-1}) was observed at 0000 UTC 22 January, just west of Makassar.

Figure 5 shows daily averaged integrated water vapor transport (IVT) during the Makassar flood. On 21 January, the most dominant feature was eastward transport of moisture ($400\text{--}700 \text{ kg m}^{-1} \text{ s}^{-1}$) from the Indian Ocean toward the eastern Maritime Continent. This transport was supported by the four vortices previously noted in the low level flow: two west of Sumatra, one over the Philippines and one over the Timor and Banda Seas. On 22 January, this water vapor transport was bolstered by a southward branch from the South China Sea and through the Karimata Strait associated with the cold surge. The maximum IVT exceeded $700 \text{ kg m}^{-1} \text{ s}^{-1}$ over the Java Sea, just west of southwestern Sulawesi.

The presence of the LLJ and enhanced moisture transport created favorable conditions for the development of convection and enhanced precipitation, which resulted in the devastating Makassar flood. In the following sections, the contribution from a number of processes known to modulate precipitation in the MC area will be analyzed in the context of this flooding event.

c. Interannual to seasonal precipitation drivers

During the January 2019 flood, Indian Ocean Dipole was in a neutral phase and ENSO-neutral conditions were present. Monsoonal westerlies from Sumatra to Papua New Guinea were

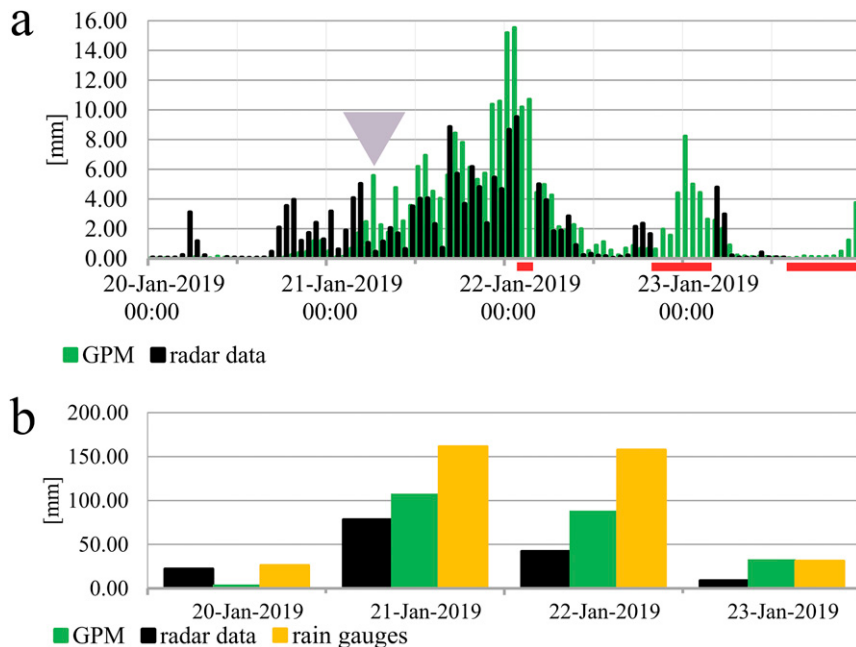


FIG. 3. (a) Mean hourly accumulated precipitation from GPM satellite and C-band Doppler radar for the flood region. Time is in UTC. Time when the dam was opened is depicted by a triangle. Red bars mark times when radar data were not available. (b) Daily mean accumulated precipitation is based on GPM satellite, radar, and 22 rain gauges. The flood zone for which both radar and GPM data are averaged over is defined as the box covering 5.05° – 5.35° S, 119.15° – 119.55° E (red box in Fig. 2).

present. On 23 January, the Australian Bureau of Meteorology (BOM) announced a weak monsoon onset in Darwin.

January 2019 sea surface temperature (SST) anomalies (Fig. 6) were positive for the most of the Maritime Continent region. In the Makassar Strait and western Indian Ocean, the SST anomalies were positive and in the range of 0° – 0.5° C, while in the Karimata Strait and South China Sea, anomalies exceeded 1° C (1° – 1.5° C). Such positive anomalies create favorable conditions for local evaporation and convection. Monthly averaged outgoing longwave radiation (OLR) values (Fig. 6) indicate areas associated with major convective regions, such as monsoon and the ITCZ. The major convection in the MC in January 2019, with very low OLR values ($<220\text{ W m}^{-2}$), was found slightly south of the equator and centered over the Java Sea. A number of studies reveal two-way feedback between convectively coupled Kelvin waves and the ITCZ (e.g., Straub and Kiladis 2002; Dias and Pauluis 2011). The location and width of ITCZ is important for wave trajectories, with the ITCZ being a waveguide for CCKWs. The flood zone was located in the southeastern part of the region of major convection.

d. Subseasonal precipitation variability

The analysis of the observed atmospheric circulation indicates the impact of various equatorial modes on the January 2019 flood event. During January 2019, an MJO event initiated over the Indian Ocean (in RMM phase 3) on 16 January (the first day when the MJO RMM index was outside the unit circle;

Fig. 7a), and then propagated eastward. By the day of the Makassar flood (21 January; red circle in Fig. 7a), the MJO was in phase 5, with enhanced convection over the Maritime Continent. This is consistent with the canonical MJO cycle, where the maximum MJO-related precipitation at Makassar is observed in phase 5 (Fig. 7b).

On 21–22 January, enhancement of total low-level wind anomalies are dominated by westerly anomalies over the Java Sea and northerly flow over the South China Sea and the Karimata Strait (Fig. 8a). The contributions to these wind anomalies from CCKWs, the MJO, and convectively coupled equatorial Rossby waves (CCERWs) are now investigated.

On 20 January, a CCKW is active with westerly anomalies over the eastern Indian Ocean and easterly anomalies over the western Maritime Continent (Fig. 8b), with a zone of convergence between these two regions. The westerly anomalies over the eastern Indian Ocean show two distinct maxima, one on the equator and one at 6° S. Over the next 2 days, this structure propagates eastward at approximately 15 m s^{-1} . The equatorial westerly anomaly decreases in magnitude, being potentially partially blocked by the mountain range on Sumatra. However, the southern branch increases in amplitude, such that the maximum precipitation at Makassar (Fig. 2) occurs in the convergence zone ahead (to the east) of it.

On 20 January, the MJO (Fig. 8c) had its maximum of low-level convergence over the Java Sea, Borneo, and Sulawesi, resulting in weak MJO-driven zonal flow in this area. On 21–22 January, the MJO low-level convergence propagated

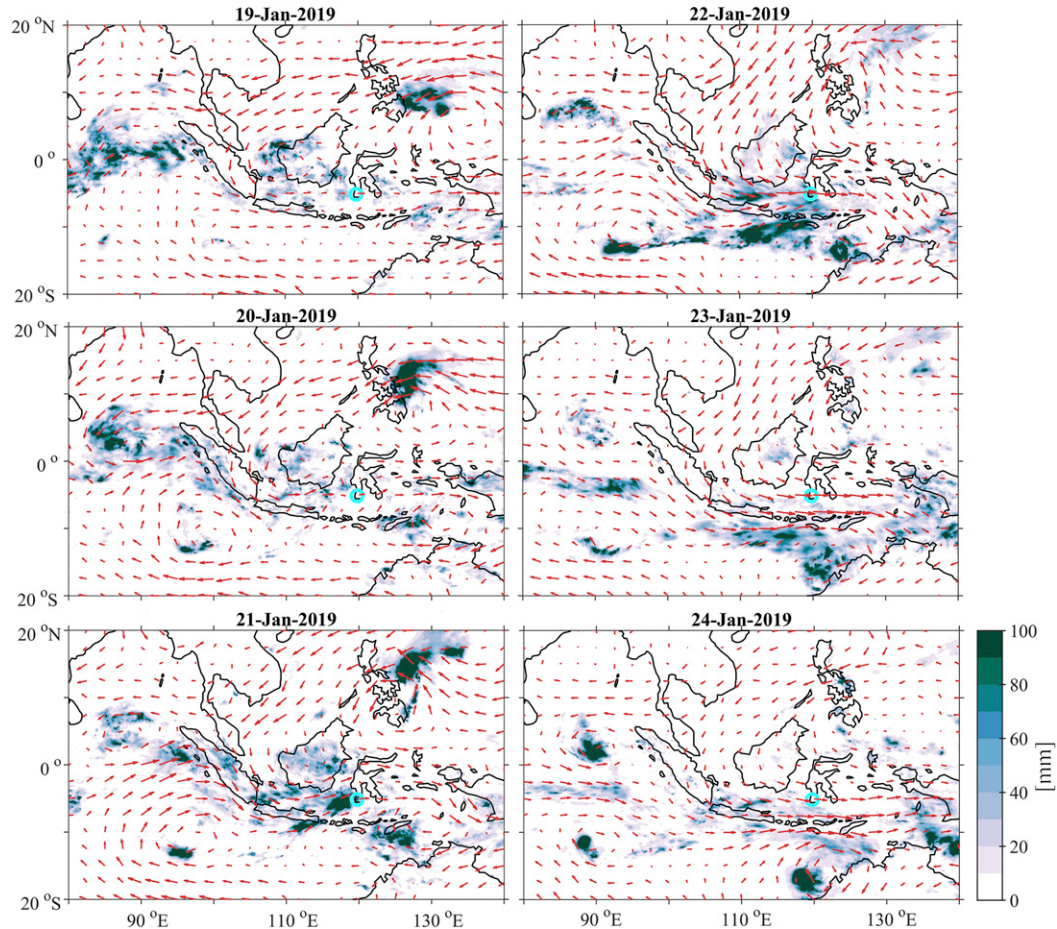


FIG. 4. Daily mean 850-hPa wind vectors and daily accumulated precipitation based on combined microwave-IR retrievals (shading, mm). The longest vector corresponds to a wind speed of 22 m s^{-1} . The flood zone is depicted by a circle.

farther east and the area of the Java Sea and South Sulawesi was affected by intraseasonal westerlies.

The bottom row in Fig. 8 shows the westward propagation of CCERWs. Of relevance to the Makassar flood is the CCERW-associated belt of westerly anomalies over the Java Sea, and the northerly anomalies over the South China Sea that can be ascribed as the cause of the cold surge there. These CCERW-associated circulation features are now shown to be the main driver of the enhanced moisture transport into the Makassar region (Fig. 5).

On 22 January 2019, total low-level wind speed anomalies over the flood zone ($5^{\circ}\text{--}6^{\circ}\text{S}$, $119^{\circ}\text{--}120^{\circ}\text{E}$) were about 12.3 m s^{-1} (Table 1). CCKW-driven anomalies with a mean speed of about 2.6 m s^{-1} account for around 21% of the total wind speed anomaly. The MJO and CCERW (2.6 and 2.0 m s^{-1}) account for about 21% and 16% of total anomalies. These three types of tropical weather systems considerably influence local low-level wind speeds by contributing 58% of total wind speed anomaly. Tropical depression-like flow and mixed Rossby-gravity wave contributions were negligible.

Figure 9 presents the zonal and meridional wind structure at 12-h resolution during January 2019, measured by radiosonde

soundings taken in Makassar, together with horizontal divergence of velocity at different levels. The arrival of the CCKW is apparent in the zonal wind structure. Before the maximum in precipitation on 22 January, weak total westerly winds are observed up to roughly 400 hPa. After 22 January, strong total westerly winds of up to 20 m s^{-1} are observed at Makassar in the lower troposphere, extending right down to the surface on 22 January itself. Hence, the lower-tropospheric convergence from the CCKW coincides with the maximum precipitation, on 22 January. The baroclinic nature of the CCKW circulation can also be seen with the strong westerlies only occupying the lower troposphere, up to 500 hPa, with strong easterly winds above. There is also a meridional component to the flow, with upper-tropospheric southerlies (upper-level divergence) observed from 22 January, likely due to a combination of the CCKW and the MJO circulation.

The large-scale convective modes that contribute to the Makassar flood on 22 January can be usefully visualized with a Hovmöller diagram of equatorial OLR anomalies (Fig. 10). Enhanced convection (negative OLR anomalies) can be seen at Makassar (119°E) on 22 January. Wavenumber-frequency

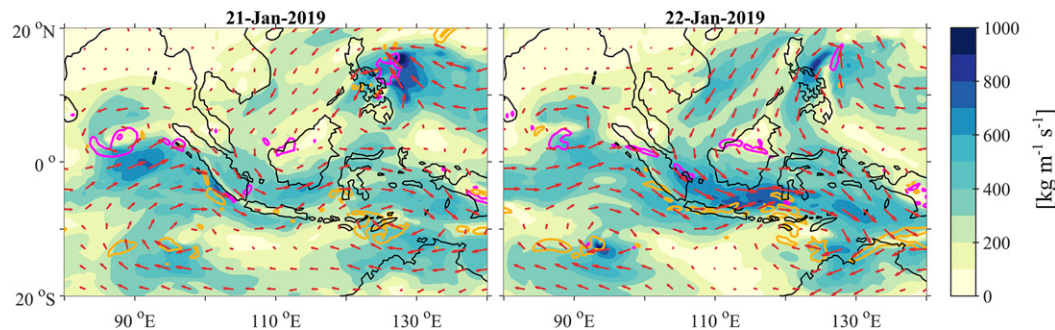


FIG. 5. Daily averaged integrated water vapor transport on 21 and 22 Jan 2019 (shading, $\text{kg m}^{-1} \text{s}^{-1}$). Daily mean values of relative vorticity at 500 hPa are superimposed (contours, s^{-1}). Pink contours show $5 \times 10^{-5} \text{s}^{-1}$ and orange contours $-5 \times 10^{-5} \text{s}^{-1}$.

filtering, as described in section 2g, shows that Makassar was under the influence of all three modes on 22 January: an eastward-propagating MJO (green contours); an eastward-propagating CCKW (black contours), and a westward-propagating CCERW (purple contours). All three of these propagating modes passed the longitude of Makassar on 22 January.

Further details of the influence of equatorial waves on rainfall distribution is depicted in Fig. 11 and in the Table 1. On 22 January, the total precipitation anomaly averaged over southwestern Sulawesi ($5^{\circ}\text{--}6^{\circ}\text{S}$, $119^{\circ}\text{--}120^{\circ}\text{E}$) was estimated at 70 mm (Fig. 11a). There were some contributions to this total anomaly from CCKW (the CCKW contribution over southwestern Sulawesi peaked on 22 January, at 8 mm, Fig. 11b) and from the MJO (5 mm, Fig. 11c). However, in the case of CCERW, both precipitation (Fig. 11d) and wind (Fig. 8d) anomalies peaked 4 days before the 22 January flood. On 22 January, the precipitation anomaly related to the CCERW over southwestern Sulawesi area was actually slightly negative. On average, the CCKW and MJO contributions to the total rainfall anomaly were 12% and 7%, respectively.

e. Mesoscale convective system

In addition to their direct contribution to the precipitation anomaly, tropical modes augment local conditions, making it favorable for multiscale convection development and further amplifying local rainfall anomalies. For the MJO and CCKW, the increase in precipitation over Sulawesi appeared closely tied to the onset of greatest low-level convergence (Fig. 9c). However, the contribution by the CCERW was more indirect. The CCERW acts to enhance the northwesterly flow from the South China Sea toward the Java Sea and contributes to the increased moisture transport (Fig. 5). Although direct CCERW-driven precipitation anomaly on the day of flood was slightly negative (-1 mm), the CCERW contribution to the anomalous moisture transport is estimated at 33% (Table 1), i.e., over twice as much as estimated for CCKW, and 80% of MJO-driven anomaly. This contribution indicates the importance of this tropical mode.

Cyclonic vorticity can also provide favorable conditions for development of mesoscale convective system (MCS) (Raymond and Jiang 1990; Davis and Trier 2002). Thus, in addition to direct contributions, the MJO and CCKW provide an environment

favorable for convection, whereas the CCERW provides enhanced low-level water vapor transport and favorable conditions for mesoscale organization.

Following the methodology described in section 2i, an MCS was detected over the Java Sea on 21 January. The system developed very rapidly, reaching the criteria for a mesoscale convective complex (MCC) (Maddox 1980). This development is consistent with the impact of equatorial waves on convective organization discussed by Yasunaga and Mapes (2012). They showed that slow, rotational waves like CCERWs contribute to an increase in environmental moisture and to the development of convective cells, while divergent waves like CCKWs promote the organization of convection into an MCS through modification of convective inhibition. Therefore, the interaction of both these modes would cause the rapid development of an MCS and increased precipitation. Indeed, this particular MCC, which developed over the Java Sea, propagated and impacted precipitation over Sulawesi, contributing over 100 mm of rainfall to the flood (Fig. 12), that is, about 60% of the total 24-h fraction of rainfall estimated by GPM IMERG. Animation of the hourly accumulated MCS-driven

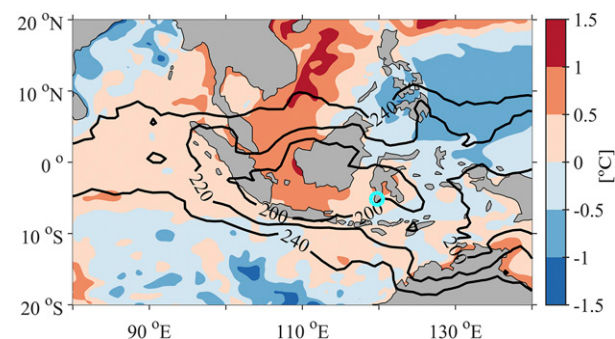


FIG. 6. January 2019 sea surface temperature (SST) anomalies. Blue shading represents negative SST anomalies and red shading represents positive anomalies. Superimposed black contours are the monthly averaged outgoing longwave radiation (OLR) values for January 2019, which are observed to be between 200 and 240 W m^{-2} . The flood zone is depicted by a circle.

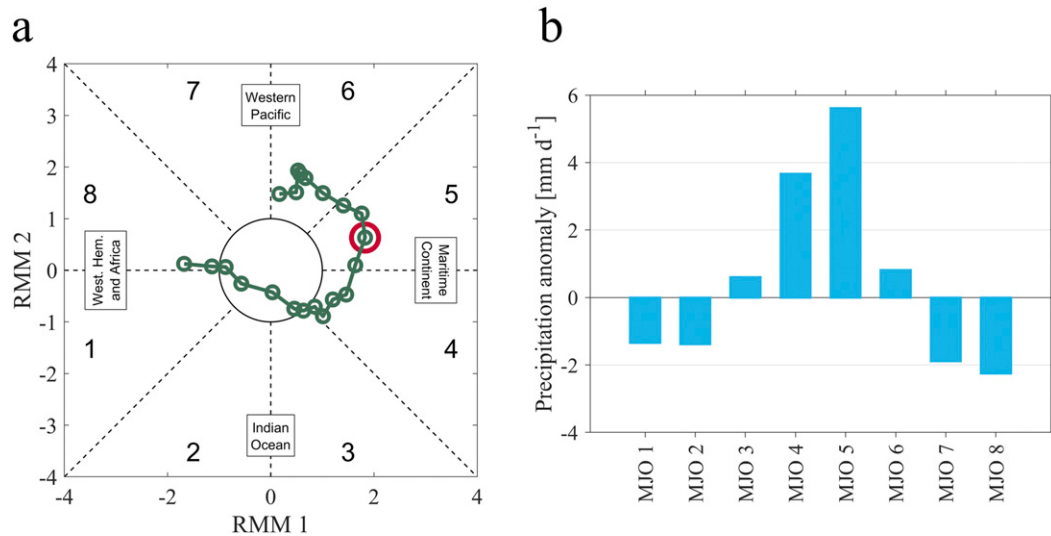


FIG. 7. (a) The Madden-Julian oscillation index in the RMM1–RMM2 phase space for 10–30 Jan 2019. The red circle indicates the Makassar flood date. (b) Precipitation anomaly during Madden-Julian oscillation active phases 1–8 in southwest Sulawesi based on in situ measurements in December, January, and February of 1998/99–2018/19.

precipitation can be found by following the link: <https://doi.org/10.6084/m9.figshare.12758744.v1> (Latos and Feng 2020).

f. Other causes of flood

Abnormally high tides attributed to the supermoon (a full moon and lunar perigee) observed on 19–22 January also contributed to the flooding. On 17 January BMKG released a warning through their social media platforms calling for coastal

communities to be aware of this danger. The water level at the mouth of the Jeneberang River rose by 0.2 m from 20 to 23 January due to this high tide (measurements taken at Makassar Maritime Meteorological Station). Strong westerly wind anomalies together with this high tide caused seawater intrusion, flooding low-lying areas in the city of Makassar.

A wind surge (cold-surge-like flow) also potentially contributed to the development of the January 2019 flood. Using

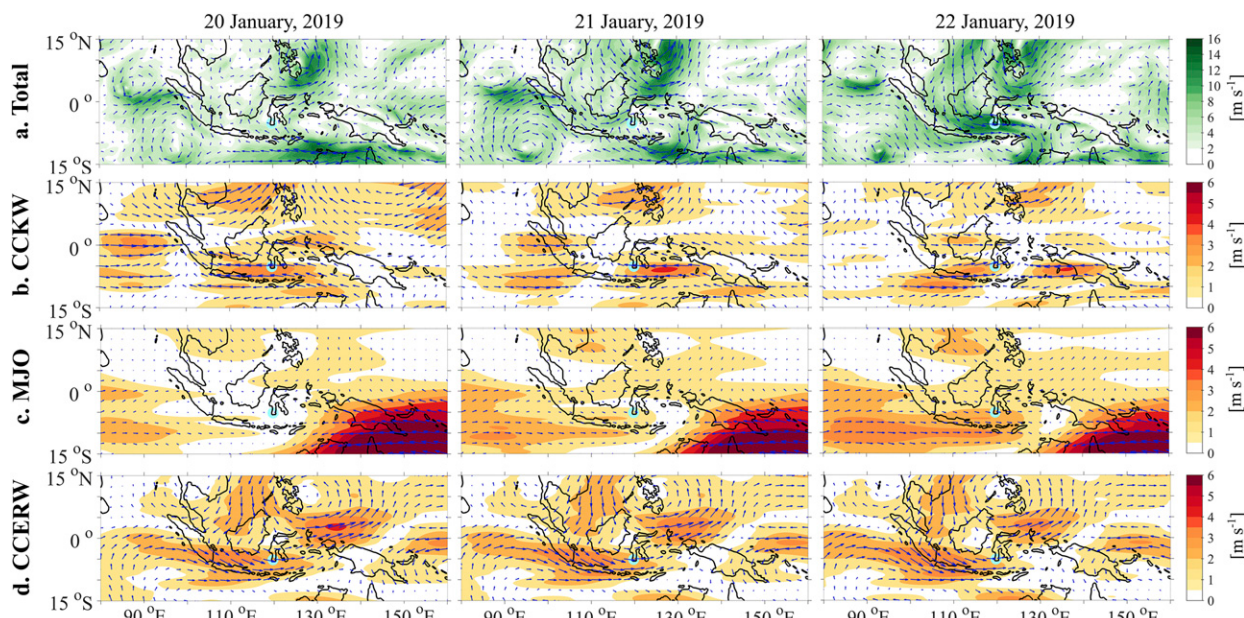


FIG. 8. Time evolution of 850-hPa wind vector anomalies during the Makassar flood event. (a) Total wind anomalies, as well as wind anomalies filtered for (b) convectively coupled Kelvin waves, (c) the Madden–Julian oscillation, and (d) convectively coupled equatorial Rossby waves. The flood zone at Makassar is shown by a blue circle.

TABLE 1. Comparison of the state of various meteorological parameters over the southwest Sulawesi region (5° – 6° S, 119° – 120° E) on 22 Jan 2019, filtered for convectively coupled equatorial Kelvin waves (CCKW), the Madden–Julian oscillation (MJO), and convectively coupled equatorial Rossby waves (CCERW).

Parameter	Total	CCKW	MJO	CCERW
IVT anomaly ($\text{kg m}^{-1} \text{s}^{-1}$)	517	70	217	173
Wind speed anomaly (m s^{-1})	12.3	2.6	2.6	2.0
Meridional wind anomaly (m s^{-1})	-1.5	-0.1	-0.2	-0.1
Zonal wind anomaly (m s^{-1})	12.2	2.6	2.6	2.0
Precipitation anomaly (mm)	70	8	5	-1

the criteria of Lim et al. (2017), which is based on wind and pressure in two rectangular boxes: 5° – 10° N, 107° – 115° E over the South China Sea and 18° – 22° N, 105° – 122° E over China, a wind surge was identified to be present on 16–18 January, and then reactivated from 21 January. The wind surge associated with the analyzed flood had the characteristics of a cross equatorial cold surge (CES) (Xavier et al. 2020), with northerly cross equatorial wind anomalies of 4 – 6 m s^{-1} . While Xavier et al. (2020) show that in January through March, CES could negatively impact the propagation of MJO in phases 2–3, during the analyzed flood the wind surge increased the moisture transport and could positively affect MJO propagation in phase 5. Intensification of the wind surge and development of the CES during the analyzed event could be also attributed to

the CCERW, which impacted the cross-equatorial flow through pressure change and circulation associated with the cyclonic vortex over the Philippines. These resulted in the intensification of northerlies over the South China Sea (Fig. 8d), considered in the surge index (Lim et al. 2017).

4. Linking equatorial waves with extreme rainfall and floods in southwest Sulawesi

a. Climatology

To understand the climatology of Sulawesi floods, we used a flood database obtained from the Indonesian National Agency for Disaster Countermeasure (BNPB). According to this database, DJF is the primary flood season with 76% of the total number of events (39 out of 51). This is in agreement with the highest precipitation rates being observed during the boreal winter months, with 65% of accumulated rainfall occurring in DJF. The majority (49%) of floods occur in January.

To explore the distribution of extreme rainfall, we used data from two stations included in the database of the Agency for Meteorology, Climatology and Geophysics of the Republic of Indonesia (BMKG), which had continuous, high quality precipitation records. We identified 49 extreme rain days, out of which 41% were associated with floods, meaning they occurred less than 2 days before the flood or within 1 day after. In addition, 51% of floods were associated with extreme rain events—they occurred less than 2 days before or within 1 day

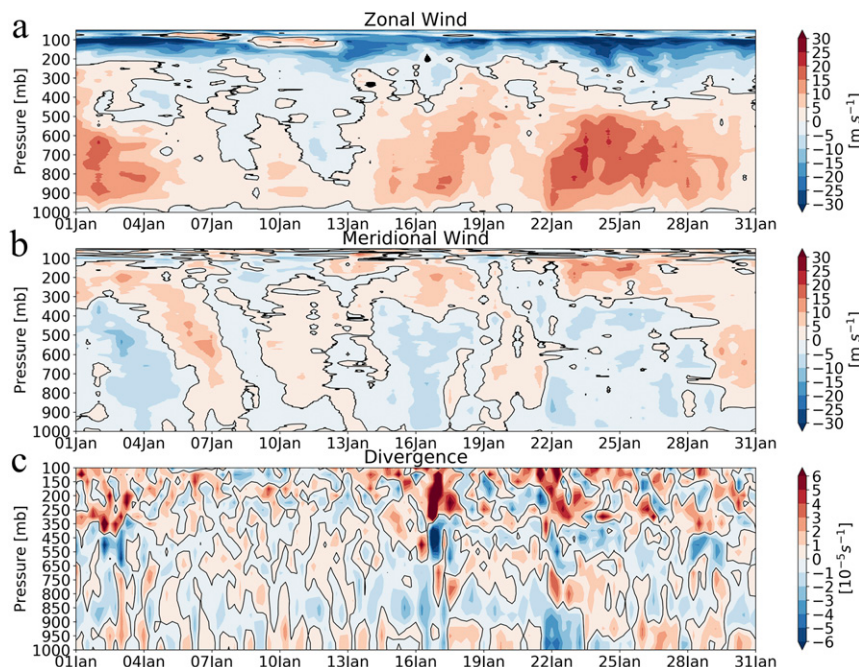


FIG. 9. Pressure vs time plots of the (a) zonal and (b) meridional components of the wind based on soundings taken in Makassar during January 2019 and (c) ERA5 horizontal divergence of velocity. The parameter in (c) is positive for air that is spreading out (divergence), and negative for air that is concentrating (convergence). The contour shading interval is (a),(b) 5 m s^{-1} and (c) 10^{-5} s^{-1} . The zero contour is emphasized by a solid black line.

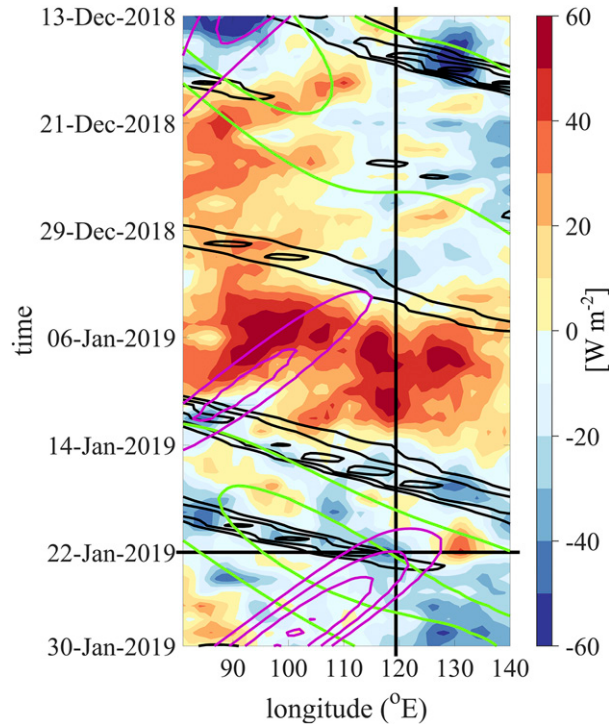


FIG. 10. Time-longitude (Hovmöller) diagram of OLR anomalies averaged over 5°N – 5°S , with an interval of 10 W m^{-2} (color shading). Line contours show the amplitudes of selected equatorial modes that have been wavenumber-frequency-filtered (details in section 2g): convectively coupled Kelvin wave (black lines, data averaged from 5°N to 10°S , contours from -20 to -6 W m^{-2} , every 4 W m^{-2}); convectively coupled equatorial Rossby waves (purple lines, data averaged from 5° to 20°S , contours as for CCKW); and Madden-Julian oscillation (green lines, data averaged from 15°N to 15°S , contours at -30 , -20 , and -10 W m^{-2}). The vertical line at 119.2°E marks the location of the city of Makassar. The horizontal line depicts 22 Jan 2019.

after the extreme rain day. Interestingly, extreme rain events in DJF were more evenly distributed throughout the season than floods, with 38% occurring in December, 35% in January, and 27% in February. The differences in extreme rain days and flood occurrence can be partially explained by local morphology. The two BMKG stations that were used in this paper are located in the lowlands, while floods can be associated with rain events in the upper slopes of mountainous terrain and rivers overflowing their banks. However, long-term in situ-measured rainfall data for these regions were not available.

b. Statistical link

To generalize the results of the January 2019 case study, we examine the role of convectively coupled equatorial waves (CCKWs and CCERWs) and the MJO in flood events identified in the BMKG database and in the extreme rain occurrences from the local weather stations discussed above.

We identify the days when equatorial modes were active in the vicinity of Sulawesi, using the empirical orthogonal function (EOF) decomposition of precipitation anomalies filtered

for CCKWs (Fig. 13a) and zonal wind anomalies filtered for CCERWs (Fig. 13b). We use different variables for the Kelvin and Rossby modes because, as established in the previous section, the primary contribution of CCKWs to Sulawesi floods is through precipitation in the convergence zone, while the primary CCERW contribution is through the wind field (and associated moisture advection). EOF analysis was applied to wavenumber-frequency-filtered data (Wheeler and Kiladis 1999) for boreal winter (DJF) between 1 January 1998 and 30 June 2019. In agreement with Roundy (2015), multiple EOFs were required to describe each phenomena, as they vary over a range of spatial scales. For each mode (CCKW or CCERW), two leading EOFs were extracted, as the eigenvectors of the covariance matrix with the largest eigenvalues (Fig. 13). The resulting principal component (PC) time series were used as an index of equatorial wave activity. PC1 and PC2 were used to formulate criteria for the wave activity. It is assumed that a CCKW is active in the area if the amplitude $\sqrt{(\text{PC1}^2 + \text{PC2}^2)}$ exceeded the threshold value defined by 1.5 standard deviations calculated for the entire 1998–2019 period. A similar technique was applied to ERs. As a result, 270 CCKW days and 248 CCERW days (out of 1895 DJF days in total) were identified. On 30 of these days, both CCKW and CCERW modes were observed near Sulawesi, while for 14 of these days, both waves were embedded within the active MJO envelope [phases 4–6; Wheeler and Hendon (2004)], similarly to the case analyzed in this study.

It can be seen (Fig. 13) that CCKW EOFs 1 and 2 explain 5.5% and 5.4% of the total variance, respectively, while CCERW EOFs 1 and 2 explain 12.5% and 11.6% of the total variance, respectively. Relatively low variance explained by precipitation-based EOFs in comparison with wind-based decomposition is a known caveat of this method. It results from the fundamental difference between the highly stochastic and transient nature of the precipitation field's evolution in comparison with the wind field.

In situ measurements from local BMKG stations indicate that CCKW, CCERW and MJO activity cause the increase in the local rainfall rate. While the daily mean rain accumulation for DJF is 20.8 mm , it increases to 25.9 mm for CCKW, 28.7 mm for CCERW, and 28.1 mm for MJO phases 4–6, with a maximum of 32.8 mm for phase 5.

To assess the contribution of selected meteorological drivers to DJF extreme rain and flooding events, we examined the percentage of extreme rain or flooding events that were associated with the MJO, CCKWs, CCERWs and positive anomalies of the zonal wind component. For the extreme rainfall events, 31% (15 out of 49) were associated with CCKWs, 20% with CCERWs, 49% with MJO phases 4–6, and 84% with positive anomalies of zonal wind. For the floods, results are similar: positive zonal wind anomalies were present during 87% of floods, 21% of flood events were related to CCKWs, 23% were related to CCERWs, and 51% were related to MJO. For southwestern Sulawesi, CCKWs are active during 14% of all DJF days, CCERW during 13%, and MJO during 30%, while positive zonal wind anomalies are present during 49% of days. Therefore, in this area, more equatorial waves and enhanced zonal wind events can be observed during floods and

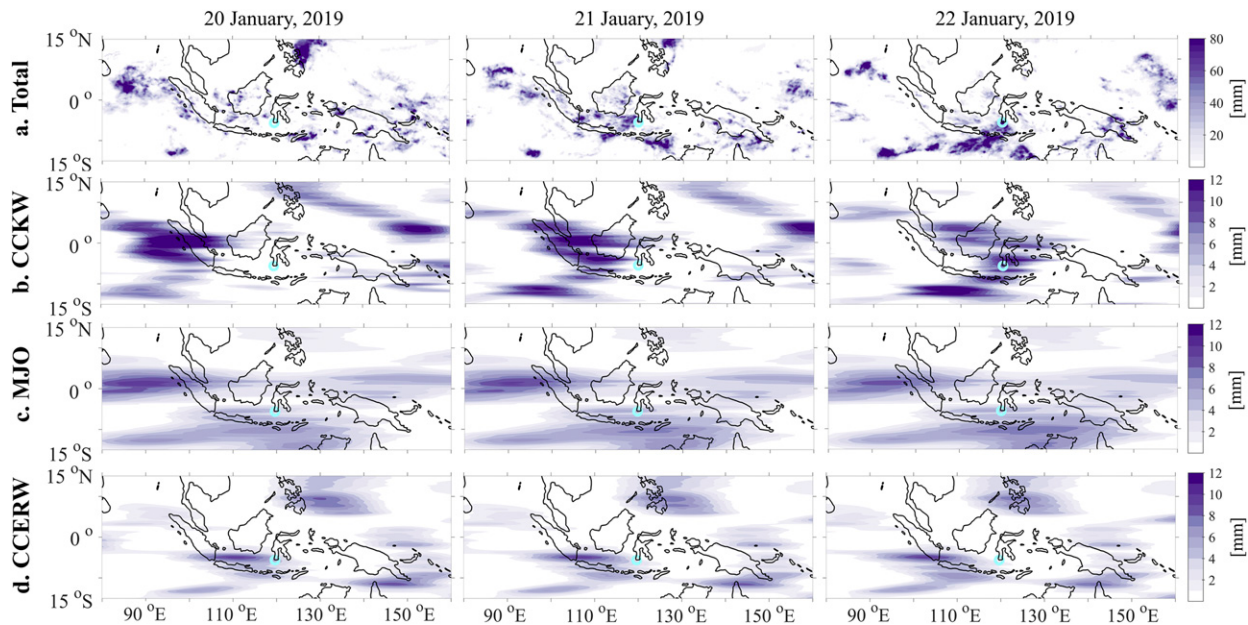


FIG. 11. Time evolution of TRMM precipitation anomalies during the January 2019 Makassar flood event: (a) total anomaly (annual cycle removed), as well as wavenumber-frequency-filtered anomalies for (b) convectively coupled Kelvin waves, (c) the Madden-Julian oscillation, and (d) convectively coupled equatorial Rossby waves. All anomalies are in mm and only positive anomalies are plotted. The shading interval for total precipitation anomalies in (a) is 4 mm and for the equatorial waves in (b)–(d) is 1 mm. The flood zone at Makassar is shown by a blue circle.

extreme rainfall than during DJF average, indicating the role of these disturbances in creating the conditions favorable for extreme precipitation and flooding.

To estimate how the presence of tropical waves increases the probability of extreme rain events and floods, we calculated the ratio of days affected by waves to total number of extreme rain and flood days. The probability of a flood on a given day during boreal winter is roughly 0.02. The chance of extreme rain is slightly higher (about 0.03). Using CCKW and CCERW identification criteria, it is estimated that the chance of CCKW or CCERW passage over Sulawesi is about 0.14. The probability of extreme rainfall during CCKW activity is about 0.06 and during CCERW activity 0.04. The probability of floods during either CCKW or CCERW is about 0.04. Therefore, these two tropical waves substantially increase the probability of natural hazard occurrence and double the chance of flood and extreme rain event development over southwestern Sulawesi. However, based on one-tailed Student's *t* test, these changes in the probability are statistically significant at an 80% confidence level only and should be considered as a rough estimation.

The probability of either extreme precipitation, flood or both occurring during joint CCKW and CCERW activity is 8 times larger than during a random DJF day. Out of 30 days of identified cases of interactions between CCKW and CCERW over Sulawesi, 5 days exhibited both flooding and extreme rain and two cases were that of extreme rain without flooding. The probability of extreme rainfall (flood) development when two interacting tropical waves are present is relatively high and equals 0.23 (0.17). Although MJO convective activity (Fig. 7b)

is an important predictor for precipitation, the probability of floods and extreme rain events within its active envelope increases significantly when CCKW and CCERW are present (from about 0.08 to about 0.2).

We have already shown that 84% of extreme rain events and 87% of Sulawesi DJF floods were preceded by positive anomalies of zonal wind. This is further confirmed in Fig. 14, which shows a composite of the time evolution of daily mean low-level (850 hPa) wind direction and wind speed anomalies during floods (first row) and during extreme rain events (second row). During the floods, westerly winds are dominating, with small contributions from other directions. Average contributions of westerly wind anomalies 2 days before, 1 day before, during, and 1 day after the flood (i.e., day -2, day -1, day 0, and day +1) are approximately 82%, 92%, 87%, and

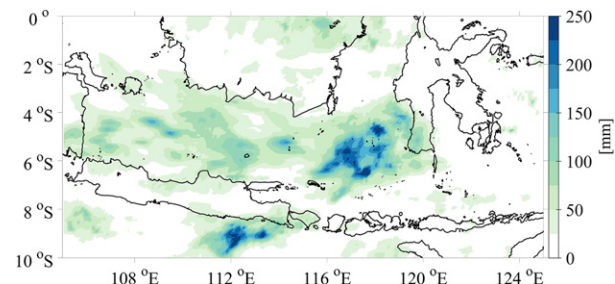


FIG. 12. Accumulated mesoscale convective systems (MCS)-driven precipitation (mm) between 0730 UTC 21 Jan and 0730 UTC 22 Jan.

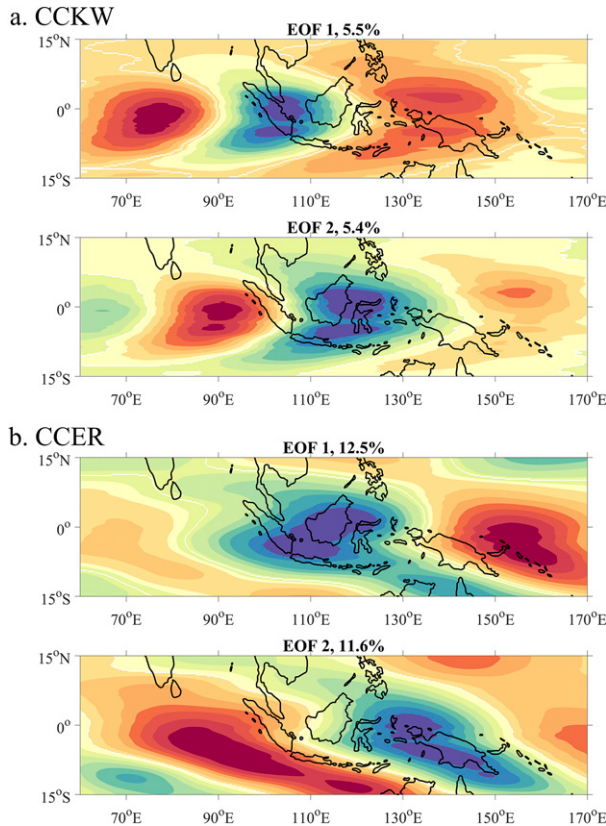


FIG. 13. The leading two EOFs of (a) convectively coupled Kelvin waves–filtered precipitation anomalies and (b) convectively coupled equatorial Rossby waves–filtered zonal wind anomalies. Red (blue) shading indicate positive (negative) values.

72%, respectively. The biggest contribution of westerlies is evident on day -1 . During extreme rain events, the average contribution of westerly wind anomalies from day -2 to day $+1$ are about 61%, 67%, 76%, and 82%, respectively. Thus, the westerly winds are present throughout the entire analyzed period; the biggest contribution is evident on day $+1$. Floods are associated with a prolonged period of anomalously strong westerlies, while extreme rain events (Fig. 14, second row) are linked to an abrupt increase of wind between day 0 and day $+1$, i.e., a 23% increase. This shows that wind convergence leads the westerly wind burst. These results suggest that floods in this area are not always preceded by extreme rainfall and that similar to Sumatra floods (Baranowski et al. 2020), rainfall accumulation in the preceding days plays an important role as well. The rainfall accumulation may be associated with longer-term convective events connected to intraseasonal variability, such as MJO or monsoon.

Figure 15 shows TRMM daily anomalous precipitation (Fig. 15a) and that decomposed for tropical modes (Fig. 15b). The precipitation anomaly peaks a day before the flood with a mean value of around 16.4 mm (Fig. 15a). A similar peak but with smaller magnitude is evident for CCKWs, suggesting that this mode is important for flood onset. A similar pattern is observed for extreme rain events (Fig. 15a), but the increase of

precipitation is much sharper and the value of precipitation is larger, reaching 35 mm. This difference in precipitation between floods and extreme rain events corresponds with what was observed for winds (Fig. 14). The MJO and CCERW impact precipitation over a slightly longer time scale. The CCERW has the largest impact on day -1 during extreme rain events and on day -3 during floods. This wave has a smaller direct impact on local rainfall variability than any other, though it has a dynamical impact, as further discussed in section 4c on the conceptual diagram.

TRMM precipitation estimates (Fig. 15a) are 2.5–3 times smaller in comparison with local mean rainfall measurements. This is a more severe underestimation of local rainfall than in the case of the January 2019 flood, where the precipitation estimated by GPM was 38% lower than measured by local rain gauges. It indicates that in this area, GPM IMERG may indeed have closer correspondence with in situ measurements than the TRMM data.

The large-scale atmospheric signal associated with floods or extreme precipitation is also seen in in situ data from local stations. Figure 15 shows the total daily precipitation anomaly before, during, and after extreme rain events (Fig. 15a) and daily average of wind speed at 10 m above the ground (Fig. 15c). The average wind speed peaks 1 day before extreme rainfall and during the flood. Maximum precipitation occurs during the flooding (41 mm on average) and during the extreme rain day (105 mm on average). The magnitude of the signal is much smaller in the case of floods, in comparison to extreme rain days. On average, long-duration rainfall accompanies both floods and extreme rainfall events. However, extreme rainfall events are associated with an abrupt increase of precipitation between day -1 and day 0. A gradual increase in clouds (Fig. 15d)—a negative sunshine duration anomaly—is evident from day -5 for floods and day -4 for extreme rain events. Therefore, the heavy rains and floods are related to longer-scale propagating atmospheric disturbances.

For both extreme rainfall and floods, MJO, CCKWs and CCERW jointly contribute about 25% of the total anomaly—that is, slightly higher than the about 20% contribution that was observed during the January 2019 case study (see section 3, Fig. 11). For that flood, a major part of the total precipitation signal was caused by the MCS that propagated from the Java Sea right over southwest Sulawesi. Since MCSs are likely to develop within the convective environment of tropical waves (Mapes et al. 2006; Yasunaga and Mapes 2012; Serra et al. 2020), one could expect a contribution from a given MCS for other floods. Some previous studies have shown that the population of MCSs within the convective MJO envelope is larger than for a suppressed MJO envelope (Xu and Rutledge 2015; Dias et al. 2017). Indeed, for DJF 2014–19, the contribution of MCSs to the total fraction of rainfall over southwestern Sulawesi increased during the presence of CCKW and CCERWs, as well as in the active phases of MJO. While the MCS-driven daily mean rain accumulation for the southwest Sulawesi is 10.4 mm, it increases to 13.3 mm when CCKW is active, 12.0 mm when CCERW is active, and 14.1 mm when MJO is in its active phases 4–6, with a maximum of 18.8 mm for

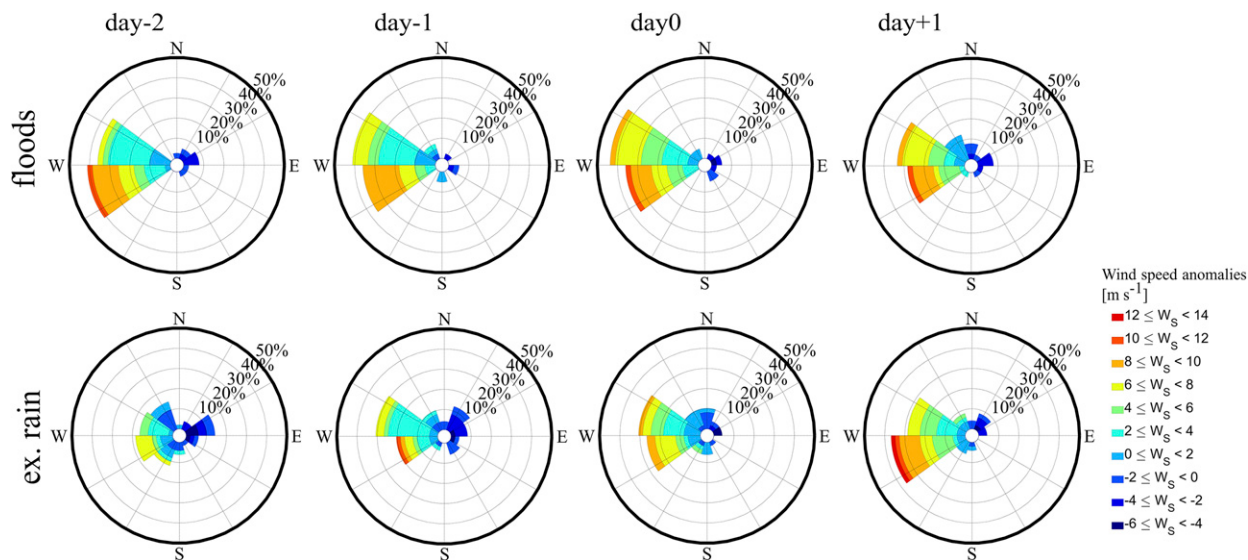


FIG. 14. Composite of time evolution of low-level (850 hPa) wind direction and wind speed anomalies during (top) floods and (bottom) extreme rain events over the southwest Sulawesi region (5° – 6° S, 119° – 120° E) during December–February of 1998/99–2018/19, plotted as wind roses. Each circle represents frequency of time that the modeled wind blows from a particular direction, changing from 0% in the center to 50% in the most outward circle. Wind speed anomalies are indicated by a color scale at an interval of $2 m s^{-1}$.

phase 5. This is a 15% increase for CCERW and 81% increase for MJO phase 5.

To estimate how the frequency and intensity of MCSs change during the presence of CCKW and CCERW, we use the phase diagram for the convectively coupled waves similar to that used by Sakaeda et al. (2020). The phase of the wave is determined based on normalized filtered precipitation (CCKW) or filtered zonal winds (CCERW) and its normalized tendency. Hourly values of filtered CCKW precipitation and CCERW westerly winds over the southwestern Sulawesi were used, together with highest precipitation MCSs that occurred during DJF 2014–19 (Fig. 16a). Additionally, to extend the analysis and generalize conclusions, we used 3-hourly TRMM satellite data and identified (section 2i) high-frequency (HF) precipitation events as a proxy of MCS for DJF 1999–2019 (Fig. 16b).

Figure 16a shows tracked highest-precipitation MCSs (hourly accumulation) as a function of the phase of a wave. The January 2019 flood is marked in green: during this flood, the highest MCS-driven precipitation occurred within moistening and wet phases of CCKW (phases 3 and 4), and strong CCERW-driven westerly wind anomalies (phase 5).

For each wave, the majority of high HF-driven precipitation events (Fig. 16b), i.e., 56%–89%, occur when CCKW normalized precipitation or CCERW normalized westerly wind anomaly is positive. This is particularly evident for CCKW.

Similarly, HF precipitation events that trigger heavy rain are more likely to develop in the moistening and wet phases of active CCKW and during increasing and strong CCERW-driven westerlies (phases 3–6 in Fig. 16b), rather than drying and dry, decreasing and weak (phases 1–2 and 7–8 in Fig. 16b). For both waves, the number of heavy precipitation events for the waves with normalized amplitude larger than 1 and in

phases 3–6 is 2–14 times greater than in phases 1–2, 7, and 8. The observed increase is the greatest for the heaviest rain events (a magnitude of precipitation of larger than three or four standard deviations) for CCKW.

c. Conceptual diagram

A conceptual diagram of meteorological conditions leading to extreme rain events and floods in southwest Sulawesi is shown in Fig. 17. The interactions between CCKWs and CCERWs within the MJO convective envelope are considered. These waves support the development of a mesoscale convective system, which in turn is responsible for extreme rainfall.

The MJO is in its enhanced convective phase over the Maritime Continent, ensuring a large-scale envelope of enhanced convection. MJO-associated lower-tropospheric westerly anomalies across the whole western Maritime Continent lead to enhanced moisture transport into the flood region. Large-scale convergence is observed ahead of the MJO active phase. Then, within this large-scale MJO envelope, a CCERW propagates westward through the region. In the meteorological situations considered here, CCERWs are dynamical precursors of extreme events, although they do not necessarily directly impact local rainfall rate on flood or extreme rain days. Their unique contribution is to support midlevel vorticity and the enhancement of northwesterly flow from the South China Sea through the Karimata Strait toward the Java Sea (a wind surge, cold-surge-like flow). Finally, CCKWs, supported by Sumatra vortices, trigger the intense convection over southwest Sulawesi in its convergence region and contribute to low-level westerly jets. All these factors cause perturbations in both dynamical and thermodynamical fields that interact with one another and contribute to MCS development and extreme rain

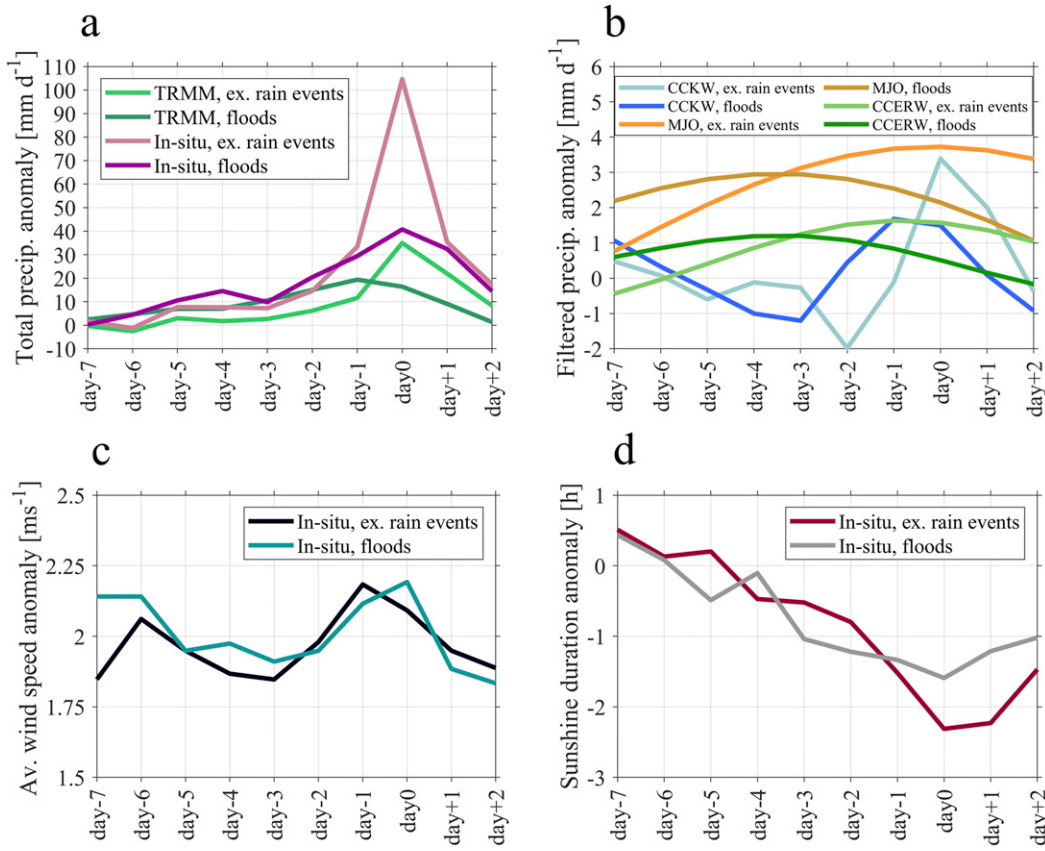


FIG. 15. (a) Total in situ–measured and satellite (TRMM) daily precipitation anomaly (mm day^{-1}) in December–February of 1998/99–2018/19 before, during, and after extreme rain events and floods in southwest Sulawesi region. (b) TRMM daily precipitation anomaly (mm day^{-1}) filtered for convectively coupled equatorial Kelvin waves (CCKW), Madden–Julian oscillation (MJO), and convectively coupled equatorial Rossby waves (CCERW). (c) Daily average of wind speed 1.5 m above the ground (m s^{-1}). (d) Daily sunshine duration anomaly (h).

or flood events. All play their own specific role in creating the perfect storm conditions; however, not all of these factors have to be present for an extreme event to occur.

5. Summary and conclusions

This study utilizes multiple sources of meteorological data to better understand the interaction among weather phenomena associated with extreme rainfall and floods in the area of southwestern Sulawesi, Indonesia, in the central Maritime Continent.

We have shown that convectively coupled equatorial waves, such as CCKWs and CCERWs embedded within the larger-scale envelope of the MJO, can provide a supportive environment for extreme weather-driven events. It appears that both CCKWs and CCERWs increase the probability of extreme rainfall and flooding. The Makassar flood of 22 January 2019, which was the largest flood ever observed in this area, is an example of the interaction of precipitation modes with different temporal and spatial scales. Besides the large-scale modes (MJO, CCERW, and CCKW), an important factor leading to this flood was the presence of a mesoscale convective

system, which contributed to a large fraction of the rainfall observed for this case. Over Indonesia, MCSs are often tied to convection over the mountains and precipitation related to these systems intensifies during interaction with CCKWs, especially for the large islands such as Sumatra or Borneo.

Pramuwardhani et al. (2020) show the increase of the afternoon (0600 UTC) and early morning (2100 UTC) precipitation maximum during the passage of Kelvin waves for Makassar as well, which indicates that Kelvin waves could contribute to flooding in southwest Sulawesi through interaction with mountain convection and enhancement of the diurnal cycle. However, while the radar observations indicated a precipitation maximum to the west of the mountain ridge (Fig. 2), the system that provided the majority of precipitation formed over the ocean in an area with CCKW-related low-level convergence (Fig. 12). Therefore, at least in this case, local diurnal precipitation did not play a major role. This is in agreement with Sakaeda et al. (2020), who show that while the majority of Sulawesi shows the “land-type” diurnal response to Kelvin waves, with intensification of the diurnal cycle ahead of wave convergence, on the southwestern tip of the island the maximum response is similar to that of the area over the ocean.

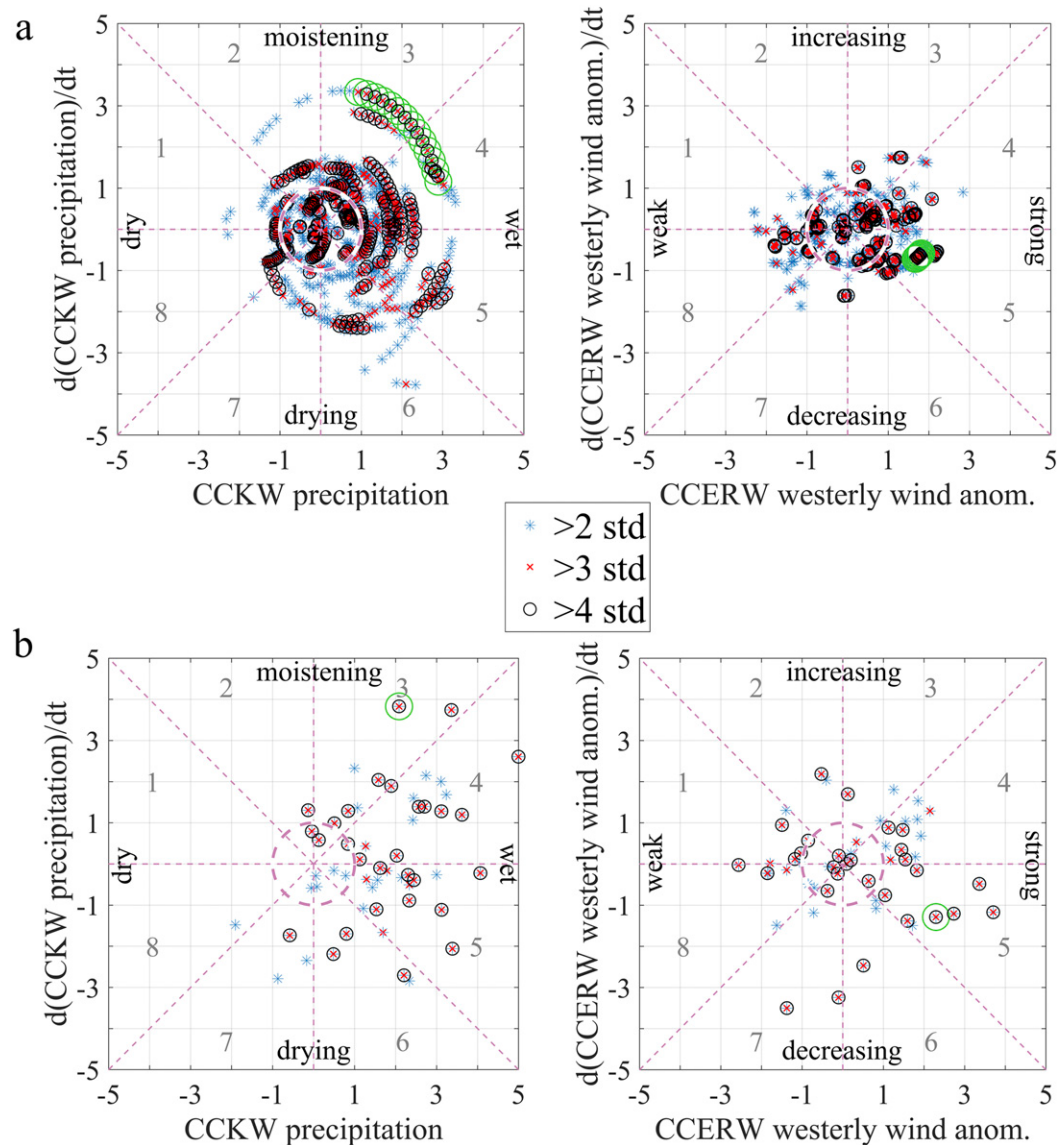


FIG. 16. (a) MCS-driven and (b) high-frequency (HF) severe precipitation with respect to (left) convectively coupled equatorial Kelvin waves (CCKWs) and (right) convectively coupled equatorial Rossby waves (CCERWs). Hours of MCS-driven precipitation in (a) and the middle of each high-frequency event in (b) that exceeded the threshold value defined by two (blue stars), three (red crosses), and four (black circles) standard deviations calculated for the entire study periods are plotted. The study period for MCSs in (a) is December–February (DJF) 2014–19, while for the study period for HF events in (b) is DJF 1999–2019. Green circles mark the January 2019 case study, analyzed in section 3. Local wave phase diagrams, adapted from Sakaeda et al. (2020), are made using hourly accumulated precipitation from GPM satellite in (a) and 3-hourly TRMM satellite precipitation in (b), filtered for CCKWs in the left panels, and (a) hourly and (b) 3-hourly westerly wind anomalies from ERA5, filtered for CCERWs in the right panels. Both wave-filtered rain rate or wave-filtered westerly wind anomaly and its tendency (the derivative of CCKW or CCERW with respect to time) are normalized by their standard deviations during the study period at each box. Negative values of the wave tendency indicate that the enhanced convective envelope of a wave is decaying and positive values indicate that it is amplifying. The southwest Sulawesi region used for calculating CCKW, MCSs, and HF-driven precipitation, as well as CCERW-driven westerly wind anomaly is defined as $4.875^{\circ}\text{--}6.125^{\circ}\text{S}$, $118.875^{\circ}\text{--}120.125^{\circ}\text{E}$.

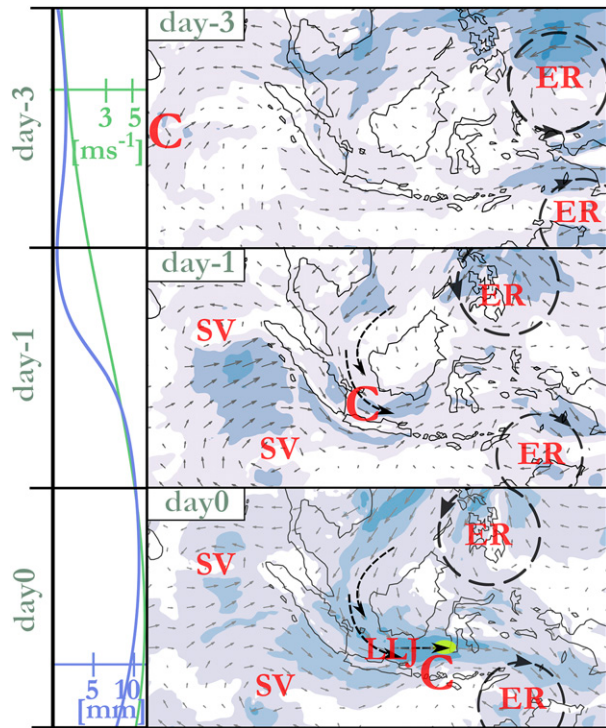


FIG. 17. (right) Schematic depiction of the key processes responsible for extreme rainfall events and floods in southwest Sulawesi (top) 3 days before (day -3), (middle) 1 day before (day -1), and (bottom) during the event (day 0). Abbreviations are as follows: C—convergence in the CCKW; ER—CCERW; LLJ—low-level jet; and SV—Sumatra vortex. The vectors and shading show winds at 850 hPa, the full-circle dashed arrows represent the equatorial Rossby wave vortices, and the curved dashed arrows represent cross-equatorial flow. The location of the meso-scale convective system is qualitatively depicted by a yellow ellipse. (left) Time evolution of approximated zonal wind anomaly (m s^{-1} , green line) and precipitation (mm, purple line) in southwest Sulawesi area.

Therefore, the precise location of precipitation related to MCSs over this region may be difficult to predict.

However, results indicate that in the studied area, the average extreme MCS-driven precipitation increases during the presence of MJO, CCKWs, and CCERWs. We also find that the population of high-frequency organized systems within the active CCKW and CCERW phase is larger than within the suppressed phase. Therefore, although the precise location of MCSs-driven precipitation is difficult to predict, examining larger-scale tropical disturbances that increase high-frequency extreme precipitation could help in more accurate predictions of future extreme precipitation and flood events. We aim to further explore the relationship between equatorial waves and higher-frequency organized tropical convection over southwestern Sulawesi in a follow-up study.

Analysis of the January 2019 case study also indicates that wind surges (Lim et al. 2017) and cross-equatorial cold surges (Xavier et al. 2020) are not in fact totally distinct features from convectively coupled equatorial waves. In this case, both

modes were potentially attributed to the CCERW-driven intensification of northerlies over the South China Sea.

Results indicate that while the MJO is a key factor for tropical predictability, consideration of the convectively coupled equatorial waves significantly increases the predictability of extreme weather. Our findings are in agreement with the conclusions of Baranowski et al. (2020) that CCKWs constitute a critical dynamical predictor for flood onset in Sumatra and Lubis and Respati (2021) that CCKWs and CCERWs increase the probability of extreme rain events over Java, as well as Ferrett et al. (2019) who link extreme precipitation in both the western and eastern parts of the Maritime Continent with high-amplitude Kelvin waves.

Our results suggest that it is possible to improve operational forecasting of extreme precipitation and floods by considering the dynamics of convectively coupled equatorially trapped waves.

Acknowledgments. This research has been supported in part by NSF Grant 1724741 “Equatorial Line Observations (ELO) field campaign during the International Years of Maritime Continent” program managed by Eric T. DeWeaver and by a subsidy of the Ministry of Education and Science in Poland for the Institute of Geophysics of the Polish Academy of Sciences. D.S.P., J.A.I.P., E.M., and E.S. were supported by the Years of Maritime Continent (YMC) project from the Indonesian Agency for Meteorology, Climatology and Geophysics (BMKG). B.L. and D.B.B. were supported by the Foundation for Polish Science. The “Multi-scale interactions over the Maritime Continent and their role in weather extremes over Central and Eastern Europe” project is carried out within the Operational Programme Smart Growth 2014–2020, Measure 4.4: Increasing the human potential in R&D sector, HOMING program of the Foundation for Polish Science co-financed by the European Union under the European Regional Development Fund. M.K.F. and J.M.S. acknowledge support from the NRL Base program PE0601153N. P.J.F. also acknowledges support from the NRL (Grant N00173-18-1-G009). Z.F. at the Pacific Northwest National Laboratory (PNNL) is supported by the U.S. Department of Energy Office of Science Biological and Environmental Research as part of the Regional and Global Modeling and Analysis program. PNNL is operated for the Department of Energy by Battelle Memorial Institute under Contract DE-AC05-76RL01830. A.J.M acknowledges support from the Natural Environment Research Council NE/R012431/1 and NE/R016704/1. ERA5, the fifth generation of ECMWF atmospheric reanalyses of the global climate, was obtained from Copernicus Climate Change Service Climate Data Store. The TRMM 3B42v7 data were provided by the NASA/Goddard Space Flight Center and PPS, which develop and compute the TRMM3B42v7 as a contribution to the TRMM project, which is archived at the NASA GES DISC. The Group for High-Resolution Sea Surface Temperature (GHRSSST) Multiscale Ultrahigh Resolution (MUR) SST data were obtained from the NASA EOSDIS Physical Oceanography Distributed Active Archive Center (PO.DAAC) at the Jet Propulsion Laboratory, Pasadena, California. We are grateful to Meteorological Service

Singapore for providing the cold surge index. We thank the two anonymous reviewers whose suggestions helped improve and clarify this manuscript.

REFERENCES

- Aldrian, E., and R. Dwi Susanto, 2003: Identification of three dominant rainfall regions within Indonesia and their relationship to sea surface temperature. *Int. J. Climatol.*, **23**, 1435–1452, <https://doi.org/10.1002/joc.950>.
- Arafat, Y., M. Saleh Pallu, F. Maricar, and R. T. Lopa, 2015: Morphology evolution of lower Jeneberang River, Indonesia. *Int. J. Earth. Sci. Eng.*, **8**, 256–258.
- Aryastana, P., T. Tanaka, and M. Mahendra, 2015: Characteristic of rainfall pattern before flood occur in Indonesia based on rainfall data from GSMAp. *Ecotrophic J. Environ. Sci.*, **7**, 100–110.
- Baranowski, D. B., M. K. Flatau, P. J. Flatau, and A. J. Matthews, 2016a: Impact of atmospheric convectively coupled equatorial Kelvin waves on upper ocean variability. *J. Geophys. Res. Atmos.*, **121**, 2045–2059, <https://doi.org/10.1002/2015JD024150>.
- , —, —, and —, 2016b: Phase locking between atmospheric convectively coupled equatorial Kelvin waves and the diurnal cycle of precipitation over the Maritime Continent. *Geophys. Res. Lett.*, **43**, 8269–8276, <https://doi.org/10.1002/2016GL069602>.
- , D. E. Waliser, X. Jiang, J. A. Ridout, and M. K. Flatau, 2019: Contemporary GCM fidelity in representing the diurnal cycle of precipitation over the Maritime Continent. *J. Geophys. Res. Atmos.*, **124**, 747–769, <https://doi.org/10.1029/2018JD029474>.
- , and Coauthors, 2020: Social-media and newspaper reports reveal large-scale meteorological drivers of floods on Sumatra. *Nat. Commun.*, **11**, 2503, <https://doi.org/10.1038/s41467-020-16171-2>.
- Berg, W., T. L'Ecuyer, and C. Kummerow, 2006: Rainfall climate regimes: The relationship of regional TRMM rainfall biases to the environment. *J. Appl. Meteor. Climatol.*, **45**, 434–454, <https://doi.org/10.1175/JAM2331.1>.
- Birch, C. E., S. Webster, S. C. Peatman, D. J. Parker, A. J. Matthews, Y. Li, and M. E. Hassim, 2016: Scale interactions between the MJO and the western maritime continent. *J. Climate*, **29**, 2471–2492, <https://doi.org/10.1175/JCLI-D-15-0557.1>.
- BMKG, 2019: Online database. Agency for Meteorology, Climatology and Geophysics of the Republic of Indonesia [Badan Meteorologi, Klimatologi, dan Geofisika (BMKG)], accessed 24 October 2019, <http://dataonline.bmkg.go.id/>.
- BNPB, 2019: Online database. Indonesian National Agency for Disaster Countermeasure [Badan Nasional Penanggulangan Bencana (BNPB)], accessed 15 March 2019, <http://bnpb.cloud/dibi/tabel1b>.
- Central Bureau of Statistics, 2017: Population of Makassar. Central Bureau of Statistics (Badan Pusat Statistik), accessed 18 November 2019, <https://makassarkota.bps.go.id/statictable/2017/04/26/6/jumlah-penduduk-kota-makassar-menurut-kecamatan-tahun-2016.html>.
- Chang, C. P., Z. Wang, J. McBride, and C. H. Liu, 2005: Annual cycle of Southeast Asia–Maritime Continent rainfall and the asymmetric monsoon transition. *J. Climate*, **18**, 287–301, <https://doi.org/10.1175/JCLI-3257.1>.
- Chen, W. T., S. P. Hsu, Y. H. Tsai, and C. H. Sui, 2019: The influences of convectively coupled Kelvin waves on multiscale rainfall variability over the South China Sea and Maritime Continent in December 2016. *J. Climate*, **32**, 6977–6993, <https://doi.org/10.1175/JCLI-D-18-0471.1>.
- Condom, T., P. Rau, and J. C. Espinoza, 2011: Correction of TRMM 3B43 monthly precipitation data over the mountainous areas of Peru during the period 1998–2007. *Hydrolog. Processes*, **25**, 1924–1933, <https://doi.org/10.1002/hyp.7949>.
- Copernicus Climate Change Service, (C3S), 2017: ERA5: Fifth generation of ECMWF atmospheric reanalyses of the global climate. Copernicus Climate Change Service Climate Data Store (CDS), accessed 14 May 2019, <https://cds.climate.copernicus.eu/cdsapp#!/home>.
- Davis, C. A., and S. B. Trier, 2002: Cloud-resolving simulations of mesoscale vortex intensification and its effect on a serial mesoscale convective system. *Mon. Wea. Rev.*, **130**, 2839–2858, [https://doi.org/10.1175/1520-0493\(2002\)130<2839:CRSOMV>2.0.CO;2](https://doi.org/10.1175/1520-0493(2002)130<2839:CRSOMV>2.0.CO;2).
- Dias, J., and O. Pauluis, 2011: Modulations of the phase speed of convectively coupled Kelvin waves by the ITCZ. *J. Atmos. Sci.*, **68**, 1446–1459, <https://doi.org/10.1175/2011JAS3630.1>.
- , N. Sakaeda, G. N. Kiladis, and K. Kikuchi, 2017: Influences of the MJO on the space-time organization of tropical convection. *J. Geophys. Res. Atmos.*, **122**, 8012–8032, <https://doi.org/10.1002/2017JD026526>.
- Feng, Z., L. R. Leung, R. A. Houze Jr., S. Hagos, J. Hardin, Q. Yang, B. Han, and J. Fan, 2018: Structure and evolution of mesoscale convective systems: Sensitivity to cloud micro-physics in convection-permitting simulations over the United States. *J. Adv. Model. Earth Syst.*, **10**, 1470–1494, <https://doi.org/10.1029/2018MS001305>.
- , and Coauthors, 2021: A global high-resolution mesoscale convective system database using satellite-derived cloud tops, surface precipitation, and tracking. *J. Geophys. Res. Atmos.*, <https://doi.org/10.1029/2020JD034202>, in press.
- Ferrett, S., G. Yang, S. Woolnough, J. Methven, K. Hodges, and C. Holloway, 2019: Linking extreme precipitation in Southeast Asia to equatorial waves. *Quart. J. Roy. Meteor. Soc.*, **146**, 665–684, <https://doi.org/10.1002/qj.3699>.
- Fine, C. M., R. H. Johnson, P. E. Ciesielski, and R. K. Taft, 2016: The role of topographically induced vortices in tropical cyclone formation over the Indian Ocean. *Mon. Wea. Rev.*, **144**, 4827–4847, <https://doi.org/10.1175/MWR-D-16-0102.1>.
- Gabella, M., and R. Notarpietro, 2002: Ground clutter characterization and elimination in mountainous terrain. *Second European Conf. on Radar Meteorology*, Delft, Netherlands, European Meteorological Society and Copernicus Gesellschaft mbH, 305–311.
- GHRSSST, 2019: The Group for High Resolution Sea Surface Temperature (GHRSSST) Multiscale Ultrahigh Resolution (MUR) SST data. JPL MUR MEaSUREs Project, accessed 5 June 2019, <https://podaac-opendap.jpl.nasa.gov/opendap/allData/ghrssst/data/GDS2/L4/GLOB/JPL/MUR/v4.1>.
- Guo, Y., X. Jiang, and D. E. Waliser, 2014: Modulation of the convectively coupled Kelvin waves over South America and the tropical Atlantic Ocean in association with the Madden-Julian oscillation. *J. Atmos. Sci.*, **71**, 1371–1388, <https://doi.org/10.1175/JAS-D-13-0215.1>.
- Heistermann, M., S. Jacobi, and T. Pfaff, 2013: An open source library for processing weather radar data (wradlib). *Hydrolog. Earth Syst. Sci.*, **17**, 863–871, <https://doi.org/10.5194/hess-17-863-2013>.
- Huffman, G. J., R. F. Adler, D. T. Bolvin, and E. J. Nelkin, 2010: The TRMM Multi-satellite Precipitation Analysis (TMPA). *Satellite Rainfall Applications for Surface Hydrology*,

- M. Gebremichael and F. Hossain, Eds., Springer, 3–22, https://doi.org/10.1007/978-90-481-2915-7_1.
- , D. Bolvin, D. Braithwaite, K. Hsu, R. Joyce, and P. Xie, 2014: NASA Global Precipitation Measurement Integrated Multisatellite Retrievals for GPM (IMERG). Algorithm Theoretical Basis Doc., version 4.4, 30 pp., https://pps.gsfc.nasa.gov/Documents/IMERG_ATBD_V4.pdf.
- , D. T. Stocker, E. J. Bolvin, J. T. Nelkin, and T. Jackson, 2019: GPM IMERG Final Precipitation L3 Half Hourly 0.1 degree × 0.1 degree V06. Goddard Earth Sciences Data and Information Services Center (GES DISC), accessed 30 September 2019, <https://doi.org/10.5067/GPM/IMERG/3B-HH/06>.
- Janowiak, J. E., R. J. Joyce, and Y. Yarosh, 2001: A real-time global half-hourly pixel-resolution infrared dataset and its applications. *Bull. Amer. Meteor. Soc.*, **82**, 205–218, [https://doi.org/10.1175/1520-0477\(2001\)082<0205:ARTGHH>2.3.CO;2](https://doi.org/10.1175/1520-0477(2001)082<0205:ARTGHH>2.3.CO;2).
- Jia, X., J. Ge, and S. Wang, 2016: Diverse impacts of ENSO on wintertime rainfall over the Maritime Continent. *Int. J. Climatol.*, **36**, 3384–3397, <https://doi.org/10.1002/joc.4562>.
- Johnson, S. J., and Coauthors, 2016: The resolution sensitivity of the South Asian monsoon and Indo-Pacific in a global 0.35 AGCM. *Climate Dyn.*, **46**, 807–831, <https://doi.org/10.1007/s00382-015-2614-1>.
- Jongman, B., H. C. Winsemius, J. C. J. H. Aerts, E. Coughlan de Perez, M. K. van Aalst, W. Kron, and P. J. Ward, 2015: Declining vulnerability to river floods and the global benefits of adaptation. *Proc. Natl. Acad. Sci. USA*, **112**, E2271–E2280, <https://doi.org/10.1073/pnas.1414439112>.
- Kiladis, G. N., K. H. Straub, and P. T. Haertel, 2005: Zonal and vertical structure of the Madden-Julian oscillation. *J. Atmos. Sci.*, **62**, 2790–2809, <https://doi.org/10.1175/JAS3520.1>.
- , M. C. Wheeler, P. T. Haertel, K. H. Straub, and P. E. Roundy, 2009: Convectively coupled equatorial waves. *Rev. Geophys.*, **47**, RG2003, <https://doi.org/10.1029/2008RG000266>.
- Krämer, S., and H. R. Verworn, 2009: Improved radar data processing algorithms for quantitative rainfall estimation in real time. *Water Sci. Technol.*, **60**, 175–184, <https://doi.org/10.2166/wst.2009.282>.
- Kripalani, R. H., and A. Kulkarni, 1997: Rainfall variability over South-east Asia—Connections with Indian monsoon and ENSO extremes: New perspectives. *Int. J. Climatol.*, **17**, 1155–1168, [https://doi.org/10.1002/\(SICI\)1097-0088\(199709\)17:11<1155::AID-JOC188>3.0.CO;2-B](https://doi.org/10.1002/(SICI)1097-0088(199709)17:11<1155::AID-JOC188>3.0.CO;2-B).
- Latos, B., and Z. Feng, 2020: Mesoscale convective systems-driven precipitation over the central Maritime Continent during January 21–22, 2019. Figshare, accessed 4 September 2020, <https://doi.org/10.6084/m9.figshare.12758744.v1>.
- , and D. Permana, 2020: The maximum of the PPI reflectivity estimated by C-band Doppler radar located in Maros, southwest Sulawesi during January 20–23, 2019. Figshare, accessed 4 September 2020, <https://doi.org/10.6084/m9.figshare.12758741.v1>.
- Liao, Z., Y. Hong, J. Wang, H. Fukuoka, K. Sassa, D. Karnawati, and F. Fathani, 2010: Prototyping an experimental early warning system for rainfall-induced landslides in Indonesia using satellite remote sensing and geospatial datasets. *Landslides*, **7**, 317–324, <https://doi.org/10.1007/s10346-010-0219-7>.
- Liebmann, B., and C. A. Smith, 1996: Description of a complete (interpolated) OLR dataset. *Bull. Amer. Meteor. Soc.*, **77**, 1275–1277.
- Lim, S. Y., C. Marzin, P. Xavier, C. P. Chang, and B. Timbal, 2017: Impacts of boreal winter monsoon cold surges and the interaction with MJO on Southeast Asia rainfall. *J. Climate*, **30**, 4267–4281, <https://doi.org/10.1175/JCLI-D-16-0546.1>.
- Love, B. S., A. J. Matthews, and G. M. Lister, 2011: The diurnal cycle of precipitation over the Maritime Continent in a high-resolution atmospheric model. *Quart. J. Roy. Meteor. Soc.*, **137**, 934–947, <https://doi.org/10.1002/qj.809>.
- Lubis, S. W., and C. Jacobi, 2015: The modulating influence of convectively coupled equatorial waves (CCEWs) on the variability of tropical precipitation. *Int. J. Climatol.*, **35**, 1465–1483, <https://doi.org/10.1002/joc.4069>.
- , and M. R. Respati, 2021: Impacts of convectively coupled equatorial waves on rainfall extremes in Java, Indonesia. *Int. J. Climatol.*, **41**, 2418–2440, <https://doi.org/10.1002/joc.6967>.
- Madden, R. A., and P. R. Julian, 1972: Description of global-scale circulation cells in the tropics with a 40–50 day period. *J. Atmos. Sci.*, **29**, 1109–1123, [https://doi.org/10.1175/1520-0469\(1972\)029<1109:DOGSCC>2.0.CO;2](https://doi.org/10.1175/1520-0469(1972)029<1109:DOGSCC>2.0.CO;2).
- Maddox, R. A., 1980: Mesoscale convective complexes. *Bull. Amer. Meteor. Soc.*, **61**, 1374–1387, [https://doi.org/10.1175/1520-0477\(1980\)061<1374:MCC>2.0.CO;2](https://doi.org/10.1175/1520-0477(1980)061<1374:MCC>2.0.CO;2).
- Mahmud, M. R., M. Hashim, and M. N. M. Reba, 2017: How effective is the new generation of GPM satellite precipitation in characterizing the rainfall variability over Malaysia? *Asia-Pac. J. Atmos. Sci.*, **53**, 375–384, <https://doi.org/10.1007/s13143-017-0042-3>.
- Majda, A. J., B. Khouider, G. N. Kiladis, K. H. Straub, and M. G. Shefter, 2004: A model for convectively coupled tropical waves: Nonlinearity, rotation, and comparison with observations. *J. Atmos. Sci.*, **61**, 2188–2205, [https://doi.org/10.1175/1520-0469\(2004\)061<2188:AMFCCT>2.0.CO;2](https://doi.org/10.1175/1520-0469(2004)061<2188:AMFCCT>2.0.CO;2).
- Mapes, B., S. Tulich, J. Lin, and P. Zuidema, 2006: The mesoscale convection life cycle: Building block or prototype for large-scale tropical waves? *Dyn. Atmos. Oceans*, **42**, 3–29, <https://doi.org/10.1016/j.dynatmoce.2006.03.003>.
- Marshall, J. S., R. C. Langille, and W. M. K. Palmer, 1947: Measurement of rainfall by radar. *J. Meteor.*, **4**, 186–192, [https://doi.org/10.1175/1520-0469\(1947\)004<0186:MORBR>2.0.CO;2](https://doi.org/10.1175/1520-0469(1947)004<0186:MORBR>2.0.CO;2).
- Matthews, A. J., G. Pickup, S. C. Peatman, P. Clews, and J. Martin, 2013: The effect of the Madden-Julian Oscillation on station rainfall and river level in the Fly River system, Papua New Guinea. *J. Geophys. Res. Atmos.*, **118**, 10 926–10 935, <https://doi.org/10.1002/jgrd.50865>.
- Measey, M., 2010: Indonesia: A vulnerable country in the face of climate change. *Global Maj. E-J.*, **1**, 31–45.
- Moron, V., A. W. Robertson, J. H. Qian, and M. Ghil, 2015: Weather types across the Maritime Continent: From the diurnal cycle to interannual variations. *Front. Environ. Sci.*, **2**, 65, <https://doi.org/10.3389/fenvs.2014.00065>.
- Muis, S., B. Güneralp, B. Jongman, J. C. Aerts, and P. J. Ward, 2015: Flood risk and adaptation strategies under climate change and urban expansion: A probabilistic analysis using global data. *Sci. Total Environ.*, **538**, 445–457, <https://doi.org/10.1016/j.scitotenv.2015.08.068>.
- Paski, J. A. I., I. J. Saragih, D. S. Permana, M. I. Hastuti, A. Kristianto, and E. E. Makmur, 2019: Simulation of land-sea breeze effect on the diurnal cycle of convective activity in the Eastern Coast of North Sumatra using WRF model. *2019 IEEE Asia-Pacific Conf. on Geoscience, Electronics and Remote Sensing Technology (AGERS)*, Jakarta, Indonesia, IEEE, 67–71, <https://doi.org/10.1109/AGERS48446.2019.9034301>.

- , F. Alfahmi, D. S. Permana, and E. E. S. Makmur, 2020: Reconstruction of extreme rainfall event on September 19–20, 2017, using a weather radar in Bengkulu of Sumatra island. *Sci. World J.*, **2020**, 1639054, <https://doi.org/10.1155/2020/1639054>.
- Paulus, A., and S. Shanas, 2017: Atmospheric study of the impact of cold surges and Borneo vortex over Western Indonesia maritime continent area. *J. Climatol. Wea. Forecasting*, **5**, 1000189, <https://doi.org/10.4172/2332-2594.1000189>.
- Pawitan, H., A. Jayawardena, K. Takeuchi, and S. Lee, 2002: Jeneberang River. *Catalogue of Rivers for Southeast Asia and the Pacific*, R. Ibbitt et al., Eds., Vol IV, The UNESCO-IHP Regional Steering Committee for Southeast Asia and the Pacific, 63–74.
- Peatman, S. C., A. J. Matthews, and D. P. Stevens, 2014: Propagation of the Madden-Julian Oscillation through the Maritime Continent and scale interaction with the diurnal cycle of precipitation. *Quart. J. Roy. Meteor. Soc.*, **140**, 814–825, <https://doi.org/10.1002/qj.2161>.
- Pramuwardani, I., H. Sunarto, and A. Sopaheluwakan, 2020: The interaction between local factors and the convectively coupled equatorial waves over Indonesia during the western North Pacific and Australian monsoon phase. *Meteor. Hydrol. Water Manage.*, **8**, 84–89.
- PUPR, 2019: Indonesian Directorate General of Water Resources. Ministry of Public Works and Public Housing [Gedung Ditjen Sumber Daya Air, Kementerian (PUPR)], The Communication Bureau (Biro Komunikasi Publik), accessed 3 October 2019, <http://sda.pu.go.id/>.
- Qian, J.-H., 2008: Why precipitation is mostly concentrated over islands in the Maritime Continent. *J. Atmos. Sci.*, **65**, 1428–1441, <https://doi.org/10.1175/2007JAS2422.1>.
- , 2020: Mechanisms for the dipolar patterns of rainfall variability over large islands in the Maritime Continent associated with the Madden-Julian oscillation. *J. Atmos. Sci.*, **77**, 2257–2278, <https://doi.org/10.1175/JAS-D-19-0091.1>.
- Ramage, C. S., 1968: Role of a tropical “maritime continent” in the atmospheric circulation. *Mon. Wea. Rev.*, **96**, 365–370, [https://doi.org/10.1175/1520-0493\(1968\)096<0365:ROATMC>2.0.CO;2](https://doi.org/10.1175/1520-0493(1968)096<0365:ROATMC>2.0.CO;2).
- Rauniyar, S., A. Protat, and H. Kanamori, 2017: Uncertainties in TRMM-ERA multisatellite-based tropical rainfall estimates over the Maritime Continent. *Earth Space Sci.*, **4**, 275–302, <https://doi.org/10.1002/2017EA000279>.
- Raymond, D., and H. Jiang, 1990: A theory for long-lived mesoscale convective systems. *J. Atmos. Sci.*, **47**, 3067–3077, [https://doi.org/10.1175/1520-0469\(1990\)047<3067:ATFLMM>2.0.CO;2](https://doi.org/10.1175/1520-0469(1990)047<3067:ATFLMM>2.0.CO;2).
- Ridout, J. A., and M. K. Flatau, 2011: Convectively coupled Kelvin wave propagation past Sumatra: A June case and corresponding composite analysis. *J. Geophys. Res.*, **116**, D07106, <https://doi.org/10.1029/2010JD014981>.
- Roundy, P. E., 2008: Analysis of convectively coupled Kelvin waves in the Indian Ocean MJO. *J. Atmos. Sci.*, **65**, 1342–1359, <https://doi.org/10.1175/2007JAS2345.1>.
- , 2015: On the interpretation of EOF analysis of ENSO, atmospheric Kelvin waves, and the MJO. *J. Climate*, **28**, 1148–1165, <https://doi.org/10.1175/JCLI-D-14-00398.1>.
- , and W. M. Frank, 2004: A climatology of waves in the equatorial region. *J. Atmos. Sci.*, **61**, 2105–2132, [https://doi.org/10.1175/1520-0469\(2004\)061<2105:ACOWIT>2.0.CO;2](https://doi.org/10.1175/1520-0469(2004)061<2105:ACOWIT>2.0.CO;2).
- Ruppert, J. H., and X. Chen, 2020: Island rainfall enhancement in the Maritime Continent. *Geophys. Res. Lett.*, **47**, e2019GL086545, <https://doi.org/10.1029/2019GL086545>.
- Saji, N., B. Goswami, P. Vinayachandran, and T. Yamagata, 1999: A dipole mode in the tropical Indian Ocean. *Nature*, **401**, 360–363, <https://doi.org/10.1038/43854>.
- Sakaeda, N., G. Kiladis, and J. Dias, 2020: The diurnal cycle of rainfall and the convectively coupled equatorial waves over the Maritime Continent. *J. Climate*, **33**, 3307–3331, <https://doi.org/10.1175/JCLI-D-19-0043.1>.
- Salahuddin, A., and S. Curtis, 2011: Climate extremes in Malaysia and the equatorial South China Sea. *Global Planet. Change*, **78**, 83–91, <https://doi.org/10.1016/j.gloplacha.2011.05.001>.
- Schott, F. A., S.-P. Xie, and J. P. McCreary, 2009: Indian Ocean circulation and climate variability. *Rev. Geophys.*, **47**, RG1002, <https://doi.org/10.1029/2007RG000245>.
- Sekaranom, A. B., and H. Masunaga, 2017: Comparison of TRMM-derived rainfall products for general and extreme rains over the Maritime Continent. *J. Appl. Meteor. Climatol.*, **56**, 1867–1881, <https://doi.org/10.1175/JAMC-D-16-0272.1>.
- Serra, Y. L., A. Rowe, D. K. Adams, and G. N. Kiladis, 2020: Kelvin waves during GOAmazon and their relationship to deep convection. *J. Atmos. Sci.*, **77**, 3533–3550, <https://doi.org/10.1175/JAS-D-20-0008.1>.
- Simpson, J., T. D. Keenan, B. Ferrier, R. H. Simpson, and G. J. Holland, 1993: Cumulus mergers in the Maritime Continent region. *Meteor. Atmos. Phys.*, **51**, 73–99, <https://doi.org/10.1007/BF01080881>.
- Straub, K. H., and G. N. Kiladis, 2002: Observations of a convectively coupled Kelvin wave in the eastern Pacific ITCZ. *J. Atmos. Sci.*, **59**, 30–53, [https://doi.org/10.1175/1520-0469\(2002\)059<0030:OOACCK>2.0.CO;2](https://doi.org/10.1175/1520-0469(2002)059<0030:OOACCK>2.0.CO;2).
- Sugiarto, N., K. Ogawara, T. Tanaka, and M. S. Mahendra, 2017: Application of GSMap product and rain gauge data for monitoring rainfall condition of flood events in Indonesia. *Int. J. Environ. Geosci.*, **1**, 36–47, <https://doi.org/10.24843/ijeg.2017.v01.i01.p05>.
- Tangang, F. T., L. Juneng, E. Salimun, P. N. Vinayachandran, Y. K. Seng, C. J. C. Reason, S. K. Behera, and T. Yasunari, 2008: On the roles of the northeast cold surge, the Borneo vortex, the Madden-Julian Oscillation, and the Indian Ocean Dipole during the extreme 2006/2007 flood in southern Peninsular Malaysia. *Geophys. Res. Lett.*, **35**, L14S07, <https://doi.org/10.1029/2008GL033429>.
- Wheeler, M. C., and G. N. Kiladis, 1999: Convectively coupled equatorial waves: Analysis of clouds and temperature in the wavenumber-frequency domain. *J. Atmos. Sci.*, **56**, 374–399, [https://doi.org/10.1175/1520-0469\(1999\)056<0374:CCEWAO>2.0.CO;2](https://doi.org/10.1175/1520-0469(1999)056<0374:CCEWAO>2.0.CO;2).
- , and H. H. Hendon, 2004: An all-season real-time multivariate MJO index: Development of an index for monitoring and prediction. *Mon. Wea. Rev.*, **132**, 1917–1932, [https://doi.org/10.1175/1520-0493\(2004\)132<1917:AARMMI>2.0.CO;2](https://doi.org/10.1175/1520-0493(2004)132<1917:AARMMI>2.0.CO;2).
- , and H. Nguyen, 2015: Encyclopedia of atmospheric sciences. *Encyclopedia of Atmospheric Sciences*, 2nd ed. G. R. North, J. Pyle, and F. Zhang, Eds., Vol. 6, Academic Press, 102–112, <https://doi.org/10.1016/B978-0-444-64046-8.00067-7>.
- Xavier, P., and Coauthors, 2020: Seasonal dependence of cold surges and their interaction with the Madden-Julian oscillation over Southeast Asia. *J. Climate*, **33**, 2467–2482, <https://doi.org/10.1175/JCLI-D-19-0048.1>.
- Xu, W., and S. A. Rutledge, 2015: Morphology, intensity, and rainfall production of MJO convection: Observations from

- DYNAMO shipborne radar and TRMM. *J. Atmos. Sci.*, **72**, 623–640, <https://doi.org/10.1175/JAS-D-14-0130.1>.
- Yamanaka, M. D., S.-Y. Ogino, P.-M. Wu, H. Jun-Ichi, S. Mori, J. Matsumoto, and F. Syamsudin, 2018: Maritime Continent coastlines controlling Earth's climate. *Prog. Earth Planet. Sci.*, **5**, 21, <https://doi.org/10.1186/s40645-018-0174-9>.
- Yasunaga, K., and B. Mapes, 2012: Differences between more divergent and more rotational types of convectively coupled equatorial waves. Part II: Composite analysis based on space-time filtering. *J. Atmos. Sci.*, **69**, 17–34, <https://doi.org/10.1175/JAS-D-11-034.1>.
- Zhang, C., 2005: Madden-Julian Oscillation. *Rev. Geophys.*, **43**, RG2003, <https://doi.org/10.1029/2004RG000158>.
- Zhang, T., S. Yang, X. Jiang, and P. Zhao, 2016: Seasonal-interannual variation and prediction of wet and dry season rainfall over the Maritime Continent: Roles of ENSO and monsoon circulation. *J. Climate*, **29**, 3675–3695, <https://doi.org/10.1175/JCLI-D-15-0222.1>.